



Estimating aboveground biomass of the mangrove forests on northeast Hainan Island in China using an upscaling method from field plots, UAV-LiDAR data and Sentinel-2 imagery



Dezhi Wang^{a,b}, Bo Wan^{a,b,*}, Jing Liu^{c,d}, Yanjun Su^e, Qinghua Guo^e, Penghua Qiu^f, Xincai Wu^{a,b}

^a Faculty of Information Engineering, China University of Geosciences (Wuhan), Lumo Road 388, 430074 Wuhan, China

^b National Engineering Research Center of Geographic Information System, Lumo Road 388, 430074 Wuhan, China

^c Key Laboratory of Virtual Geographic Environment, Ministry of Education, Nanjing Normal University, Nanjing, China

^d Jiangsu Centre for Collaborative Innovation in Geographical Information Resource Development and Application, Nanjing, Jiangsu, China

^e State Key Laboratory of Vegetation and Environmental Change, Institute of Botany, Chinese Academy of Sciences, Beijing 100093, China

^f College of Geography and Environmental Science, Hainan Normal University, Longkun South Street 99, 571158 Haikou, China

ARTICLE INFO

Keywords:

Mangroves
Aboveground biomass
UAV-LiDAR
Sentinel-2
Random forest

ABSTRACT

The mangrove forests of northeast Hainan Island are the most species diverse forests in China and consist of the Dongzhai National Nature Reserve and the Qinglan Provincial Nature Reserve. The former reserve is the first Chinese national nature reserve for mangroves and the latter has the most abundant mangrove species in China. However, to date the aboveground ground biomass (AGB) of this mangrove region has not been quantified due to the high species diversity and the difficulty of extensive field sampling in mangrove habitat. Although three-dimensional point clouds can capture the forest vertical structure, their application to large areas is hindered by the logistics, costs and data volumes involved. To fill the gap and address this issue, this study proposed a novel upscaling method for mangrove AGB estimation using field plots, UAV-LiDAR strip data and Sentinel-2 imagery (named G~LiDAR~S2 model) based on a point-line-polygon framework. In this model, the partial-coverage UAV-LiDAR data were used as a linear bridge to link ground measurements to the wall-to-wall coverage Sentinel-2 data. The results showed that northeast Hainan Island has a total mangrove AGB of 312,806.29 Mg with a mean AGB of 119.26 Mg ha⁻¹. The results also indicated that at the regional scale, the proposed UAV-LiDAR linear bridge method (i.e., G~LiDAR~S2 model) performed better than the traditional approach, which directly relates field plots to Sentinel-2 data (named the G~S2 model) ($R^2 = 0.62 > 0.52$, RMSE = 50.36 Mg ha⁻¹ < 56.63 Mg ha⁻¹). Through a trend extrapolation method, this study inferred that the G~LiDAR~S2 model could decrease the number of field samples required by approximately 37% in comparison with those required by the G~S2 model in the study area. Regarding the UAV-LiDAR sampling intensity, compared with the original number of LiDAR plots, 20% of original linear bridges could produce an acceptable accuracy ($R^2 = 0.62$, RMSE = 51.03 Mg ha⁻¹). Consequently, this study presents the first investigation of AGB for the mangrove forests on northeast Hainan Island in China and verifies the feasibility of using this mangrove AGB upscaling method for diverse mangrove forests.

1. Introduction

Mangroves are salt-tolerant woody plants composed of evergreen trees and shrubs and grow in the intertidal region of the tropical and subtropical coasts with low wave energy. Mangroves are distributed in 118 countries and regions, with a total global area of approximately 137,760 km², accounting for 0.7% of the tropical forests in the world (Giri et al., 2011). Mangroves play an important role in the protection of coastal communities from storm surges and tsunamis. Mangroves

also contribute to shoreline stabilization, carbon sequestration, harboring coastal fauna and maintaining biodiversity (Duke et al., 2007). Mangrove-lined estuaries and coastal ecosystems are significant to global biogeochemical processes and they regulate the structure and function of surrounding coastal ecosystems disproportionately relative to their limited land cover (Fatoyinbo et al., 2018). Despite their ecological importance, between 35% and 60% of the world's mangrove forests have been lost since the 1950s (Fatoyinbo et al., 2018), and the mangroves in China are no exception, with a reduction of

* Corresponding author at: Faculty of Information Engineering, China University of Geosciences (Wuhan), Lumo Road 388, 430074 Wuhan, China.
E-mail address: magicwan1105@163.com (B. Wan).

approximately 50% (Liao and Zhang, 2014). Therefore, it is crucial to monitor mangrove forests and evaluate their biophysical status in response to forest ecosystem degradation and land use change.

Northeast Hainan Island has the most diverse mangrove species in China (Chen et al., 2009). This area consists of the Dongzhai Harbor National Nature Reserve (DNR) and the Qinglan Harbor Provincial Nature Reserve (QPR), which have 23 and 35 mangrove species, respectively, accounting for 95% of the Chinese mangrove species (Chen et al., 2009). There are many mangrove forests with mixed species that have epiphytic plants and vines growing over them, showing the characteristics of primeval forests. Due to the wide coverage and diverse species, northeast Hainan Island is vital for mangrove conservation in China. However, the mangrove aboveground biomass (AGB) of this region has long been neglected and to date, no study has estimated it.

Traditionally, mangrove AGB is estimated by destructive harvesting methods, which are used to develop allometric equations based on the measured parameters from these harvested trees, such as diameter at breast height (DBH), tree height and timber volume (Wen, 1999). However, when applying these allometric equations over a large area, this approach is cumbersome and sometimes impractical since the point/field measurement input parameters are difficult to obtain (Hickey et al., 2018). Remote sensing techniques can provide large-scale and accurate biophysical information for forests in an efficient and repetitive manner (Kuenzer et al., 2011). Therefore, remote sensing techniques have been widely used to estimate mangrove AGB or carbon stock in the past decade (Chadwick 2011; Fatoyinbo et al., 2018; Pereira et al., 2018; Simard et al., 2006). The main methods are statistical models that couple a certain number of ground AGB measurements with metrics extracted from coinciding remote sensing data. Subsequently, the models are extrapolated to the entire study area. For example, Pham and Brabyn (2017) utilized SPOT-4/5 data, Wicaksono et al. (2016) employed ALOS advanced visible and near infrared radiometer type 2 (AVNIR-2) data, Zhu et al. (2015) utilized WorldView-2 images, and Fatoyinbo et al. (2018) and Pereira et al. (2018) used airborne LiDAR data with a limited number of field sampling plots to retrieve mangrove AGB at the local scale.

However, when using remote sensing methods to estimate the mangrove AGB over a large area, especially for diverse and complex mangrove forests, more ground samples should be collected to cover the study area and obtain satisfactory accuracy. Nevertheless, mangroves grow in a relatively harsh environment of intertidal mudflats that are periodically inundated by seawater, with high temperature, high salinity and muddy anaerobic soils (Giri et al., 2011). Mangrove forests are also very dense. All these factors make it more difficult to access mangrove forests for extensive field surveying and sampling than terrestrial forests (Wang et al., 2018a, 2019). Alternatively, for large-scale mangrove AGB estimations, some researchers used LiDAR data to calibrate SRTM (Shuttle Radar Topography Mission) elevation data and obtained a wall-to-wall mangrove height map. The mangrove height was subsequently utilized to estimate AGB based on allometric equations. For example, Simard et al. (2006) used airborne LiDAR data to calibrate SRTM data, and Simard et al. (2008) and Fatoyinbo and Simard (2013) utilized LiDAR data from the Geoscience Laser Altimeter System (GLAS) on board the Ice, Cloud, and Land Elevation Satellite (ICESat) to calibrate SRTM data at regional scale. During this process, field plots were only used to build a simple height-to-biomass model. Therefore, there were few field samples in these studies.

Regarding the estimation of terrestrial forest attribute, LiDAR sampling (Korhonen et al., 2017; Matasci et al., 2018; Su et al., 2016; Wulder et al., 2012) and digital stereo imagery sampling (Puliti et al., 2017, 2018) have been proposed for the characterization and mapping of large-area forests, and these techniques showed great potential over the past few years, which could mitigate the costs of field plot installation and improve the precision of estimates.

LiDAR sampling involves using airborne or spaceborne LiDAR

transects as intermediate data to link ground measurements with wall-to-wall imagery. During this process, two models are created. Field measurements (various biophysical attributes such as tree height, growing stock volume or AGB) are related to LiDAR metrics. Then, LiDAR-estimated biophysical attributes or LiDAR metrics are subsequently modeled as a function of satellite metrics (Matasci et al., 2018; Wulder et al., 2012). This method could extrapolate forest biophysical parameters beyond the coverage area of LiDAR or field data to obtain a whole area of interest (Matasci et al., 2018; Nelson et al., 2017). Huang et al. (2019), for example, first retrieved the AGB of GLAS plots by coupling field-based allometric equations with forest canopy height from ICESat-GLAS data, then they linked the GLAS AGB to various predictor variables derived from wall-to-wall Landsat images and PALSAR data to produce a AGB map for the national forest at 30 m resolution. The digital stereo imagery sampling method is similar to the LiDAR sampling method because it also generates and uses point clouds.

Airborne (Liu et al., 2018a; Shao et al., 2017) and satellite LiDAR (Huang et al., 2019) are the most popular approaches to survey forest vertical structure and can also serve as intermediate data to link field samples with wall-to-wall imagery; however, LiDAR mounted on unmanned aerial vehicles (UAV-LiDAR), a state-of-the-art active remote sensing technique, has also shown great potential for use in forest inventories (Guo et al., 2017). Compared with traditional airborne and spaceborne LiDAR, UAV-LiDAR is more advantageous for capturing the fine-resolution three-dimensional structure of forests and digital terrain at low cost and with high mobility (Guo et al., 2017). For example, Liu et al. (2018b) demonstrated good performance of UAV-LiDAR in ginkgo AGB estimation. Due to these advantages and the limitation of small spatial coverage by UAVs, UAV-LiDAR may be more suitable as a sampling tool or intermediate data, especially for dispersed and elongated mangrove forests. Moreover, to date, no study has employed UAV-LiDAR data to estimate mangrove AGB.

Sentinel-2 satellite imagery is globally- and freely-available, which facilitates low-cost large-scale mangrove AGB estimation. The Sentinel-2 mission is composed of two identical satellites that were launched in 2015 and 2017, which enhances the monitoring of terrestrial and coastal ecosystems (Drusch et al., 2012; Shoko and Mutanga, 2017). The Sentinel-2 imagery has 13 multispectral bands, where three bands are red-edge spectra with spatial resolutions of 20 m and four bands are traditional spectra (red, green, blue and near infrared) with spatial resolutions of 10 m (Drusch et al., 2012). As the only freely- and globally-available multispectral imagery that provides red-edge images at present, Sentinel-2 data widen the spectral windows for forest inventories (Mura et al., 2018; Wang et al., 2018a). In addition, the two identical satellites give Sentinel-2 a short revisit period of five days and thus more possibility to produce cloud-free images. This is particularly helpful for tropical mangrove forest monitoring because clouds are frequent over mangrove areas. To the best of our knowledge, only a few publications have used Sentinel-2 imagery to retrieve mangrove AGB. For example, Castillo et al. (2017) used Sentinel-1 SAR and Sentinel-2 multispectral imagery to estimate and map mangrove AGB and their replacement land uses in the Philippines. Pham et al. (2018) utilized a combination of Sentinel-2 and ALOS-2 PALSAR-2 data to estimate the AGB of a mangrove plantation in Vietnam.

The overall aim of this study was to estimate the AGB of the mangrove forests in the northeast of Hainan Island, China. In particular, we intended to propose a novel AGB upscaling method by integrating field plots, UAV-LiDAR strip data and Sentinel-2 imagery based on a point-line-polygon framework. In this framework, the partial-coverage UAV-LiDAR strip data (line) were used to correlate field measurements (point) with wall-to-wall coverage Sentinel-2 imagery (polygon) for large-area AGB estimation. The specific objectives of the study were to (1) estimate and map the mangrove AGB of the mangrove forests on northeast Hainan Island; (2) evaluate the effectiveness of the proposed upscaling method by assessing the AGB estimation accuracy at local and

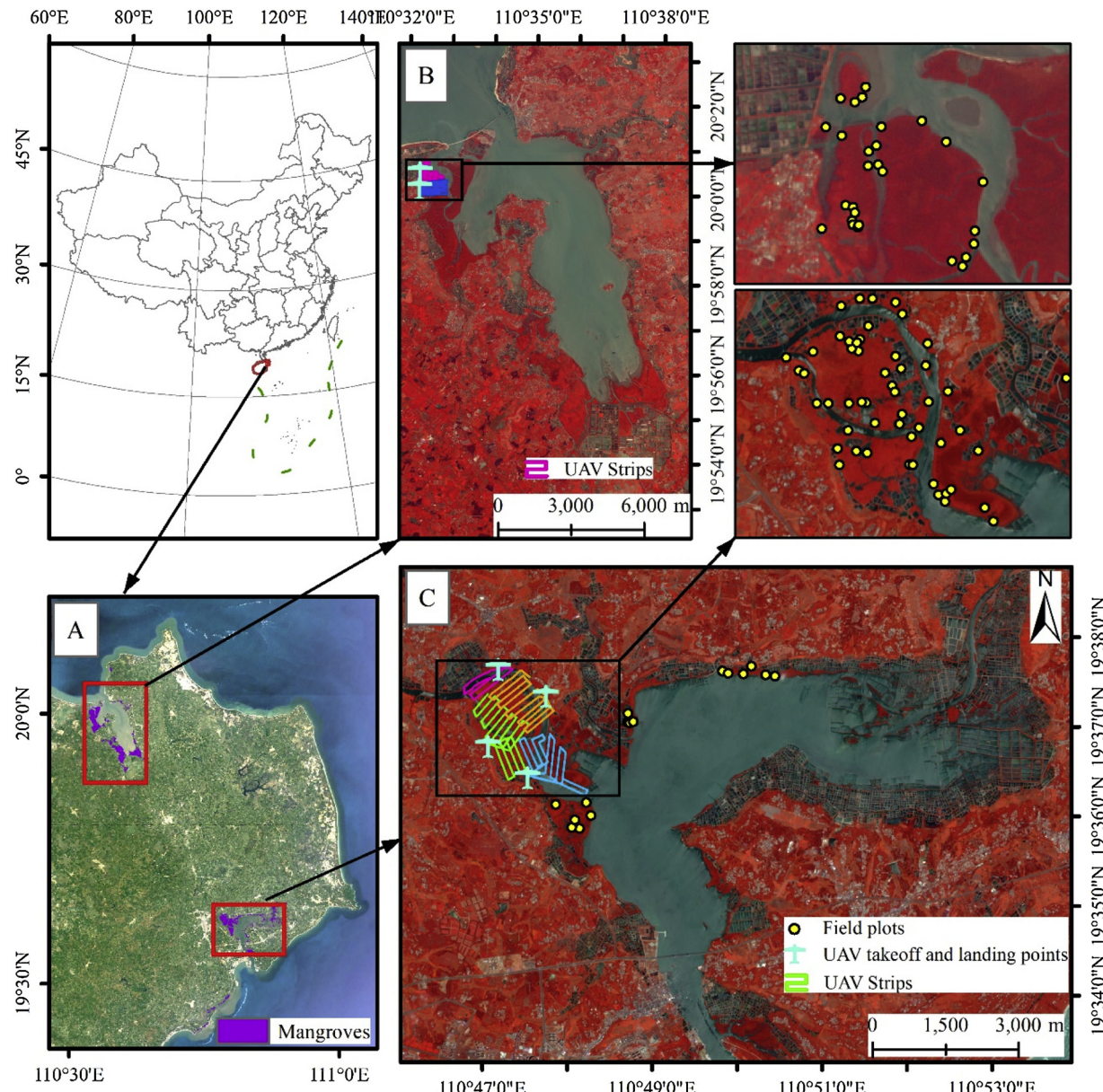


Fig. 1. The location of the study area. A: northeast Hainan island, B: the Dongzhai Harbor National Nature Reserve and C: the core area of the Qinglan Harbor Provincial Nature Reserve with the location of the 97 field plot samples.

regional scales; and (3) examine whether the inclusion of a UAV-LiDAR bridge could reduce the field sampling intensity while maintaining the estimation accuracy.

2. Data

2.1. Study area and field survey

This study was conducted on the mangrove forests of northeast Hainan Island in China (Fig. 1). This area consists of two mangrove reserves: the Qinglan Harbor Provincial Nature Reserve (QPR) and the Dongzhai Harbor National Nature Reserve (DNR). The DNR, located at 111°32' E, 20°00'N, covers a total area of 3338 ha and is the first national nature reserve and the first Ramsar Convention wetland for mangroves in China (approximately 1578 ha). The QPR has three sub-areas, namely, the Qinglan Harbor, the Fengjia Harbor, and Puqian, and its core area is located in the Qinglan Harbor (110°47' E, 19°37'N). The QPR spreads over a total area of 2948 ha and has abundant mangrove

species in China (Chen et al., 2009), where the mangrove area is approximately 1233 ha and there are 35 mangrove species. The main mangrove species in this region are *Rhizophora stylosa*, *Bruguiera sexangula*, *Ceriops tagal*, *Lumnitzera racemosa*, *Avicennia marina*, *Sonneratia* spp., *Excoecaria agallocha*, *Kandelia candel* and *Rhizophora apiculata*.

The field campaigns were conducted in late July and early August 2018 and early March 2019 (Fig. 2). There were 97 sample plots in total, of which 28 plots were located in the DNR and 69 plots were located in the QPR. All plots were square or rectangular in shape and their sizes varied from 100 m² to 600 m², depending on species composition and structure, community succession stage and the accessibility of geographical location. Within each plot, tree diameter at breast height (DBH) was measured for all trees with DBH ≥ 1.5 cm, and the species of each tree was recorded. The tree height and canopy diameter of two trees per species were also measured in each plot. The tree height was measured by using a hand-held hypsometer. The canopy diameter was obtained by using a tape measure to measure the short and long axes of a tree's vertical projection. The coordinates of the plot vertices



Fig. 2. Field survey (A and B) and UAV-LiDAR data acquisition in field (C).

Table 1

The list of the species-specific biomass allometric equations used in this study.

Species	Allometric equation	Country	Reference
<i>R. stylosa</i>	0.1050DBH ^{2.6848}	Australia	Clough and Scott (1989)
<i>B. sexangula</i>	0.168DBH ^{2.42}	Australia	Clough and Scott (1989)
<i>A. marina</i>	0.1012DBH ² + 0.5402DBH - 1.5674	China	Fan (2008)
Sonneratia spp. ^a	0.258DBH ^{2.287}	Indonesia	Kusmana et al. (2018)
<i>S. apetala</i> ^b	0.251 ρ×DBH ^{2.46}	Thailand	Komiyama et al. (2005)
<i>K. candel</i>	0.04(DBH ² * H) ^{1.0531}	China	Tam et al. (1995)
<i>R. apiculata</i>	0.235DBH ^{2.420}	Malaysia	Ong et al. (2004)
<i>E. agallocha</i>	0.1389DBH ^{2.1992}	Bangladesh	Hossain et al. (2015)
<i>C. tagal</i>	0.1885DBH ^{2.3379}	Australia	Clough and Scott, 1989
<i>L. racemosa</i>	0.1023DBH ^{2.50}	Guiana	Fromard et al. (1998)
<i>A. corniculatum</i>	0.4325(DBH ² * H) ^{0.465}	China	Tam et al. (1995)
<i>X. granatum</i>	0.0823DBH ^{2.5883}	Australia	Clough and Scott, 1989
<i>H. littoralis</i> ^c	0.251 ρ×DBH ^{2.46}	Thailand	Komiyama et al. (2005)
<i>H. tiliaceus</i> ^c		Indonesia	

where AGB is in kg, DBH is in cm, H is in m.

^a Used for all Sonneratia spp., except for *S. apetala*.

^b The ρ of *S. apetala* is 0.51, as determined by Chowdhury et al. (2013) in Bangladesh.

^c The ρ of *Heritiera littoralis* and *Hibiscus tiliaceus* are 0.6010, as determined by Jachowski et al. (2013) in Thailand.

Table 2

Summary of the field estimated aboveground biomass ($Mg\ ha^{-1}$).

Location	Number of plots	Mean	Range	Standard deviation
DNR	28	55.95	1.90 ~ 148.32	39.08
QPR	69	178.91	36.52 ~ 347.20	76.49
SUM	97	143.41	1.90 ~ 347.20	87.81

were measured using a Real-Time Kinematic Global Navigation Satellite System (RTK-GNSS) coupled with continuously operating reference stations (CORS) with centimeter-level accuracy. Species-specific biomass allometric equations (as shown in Table 1) were used to calculate the AGB of each tree. Finally, the field plot AGB density was obtained by first summing the AGB of all trees and then dividing the total by the area of the field plot. Table 2 presents a summary of the field estimated mangrove AGB in the study area.

2.2. UAV-LiDAR data acquisition and pre-processing

The UAV-LiDAR data were collected from 25 to 28 March 2018 using a low-cost and lightweight Velodyne VLP-16 Puck sensor mounted on a DJI M600 UAV. The laser sensor operates at 903 nm and has 16 scanning channels. The repetition frequency of outgoing laser pulses is 21.7 kHz. The sensor can generate a maximum of 300,000 points per second in a single return mode. The first day was used to test the equipment and explore the study area to determine the candidate UAV takeoff and landing locations. During the three following days, we carried out 6 flights in the DNR and 10 flights in the QPR and obtained

LiDAR data over a total area of approximately 450 ha. The flight speed was 5 m/s, and the flight altitude was 52 m above the ground. For each laser beam, only the strongest return was recorded. Finally, the average point density was approximately 94 points/m², and the swath width was approximately 110 m. The workflow for UAV-LiDAR data acquisition and processing is delineated in Fig. 3.

After the UAV-LiDAR survey, the raw LiDAR points, raw UAV POS data (consisting of IMU (inertial measurement unit) and GNSS data) and base station data used for ground reference were obtained. We first input the raw UAV POS data and base station data into the GNSS-Inertial processor in POSPac UAV 8.1 software (Applanix, Richmond Hill, Ontario, Canada) and obtained a smoothed best estimate of trajectory (SBET), namely, post-processed POS data. Then the raw LiDAR point data and the SBET were jointly computed to produce post-processed LiDAR point clouds with centimeter level accuracy in vertical and horizontal directions. Subsequently, the post-processed LiDAR data were denoised using LiDAR360 3.1 software (GreenValley, Being, China) to remove the noise points floating between the flight altitude and the mangroves. Finally, the point clouds were classified as ground or non-ground points using an improved TIN (triangulated irregular network) densification filtering algorithm (Zhao et al., 2016) and masked by mangrove extent polygons that were produced from Sentinel-2 imagery.

2.3. Sentinel-2 data acquisition and pre-processing

The Sentinel-2 Multispectral Instrument imagery were downloaded from the Copernicus Open Access Hub (<https://scihub.copernicus.eu/>).

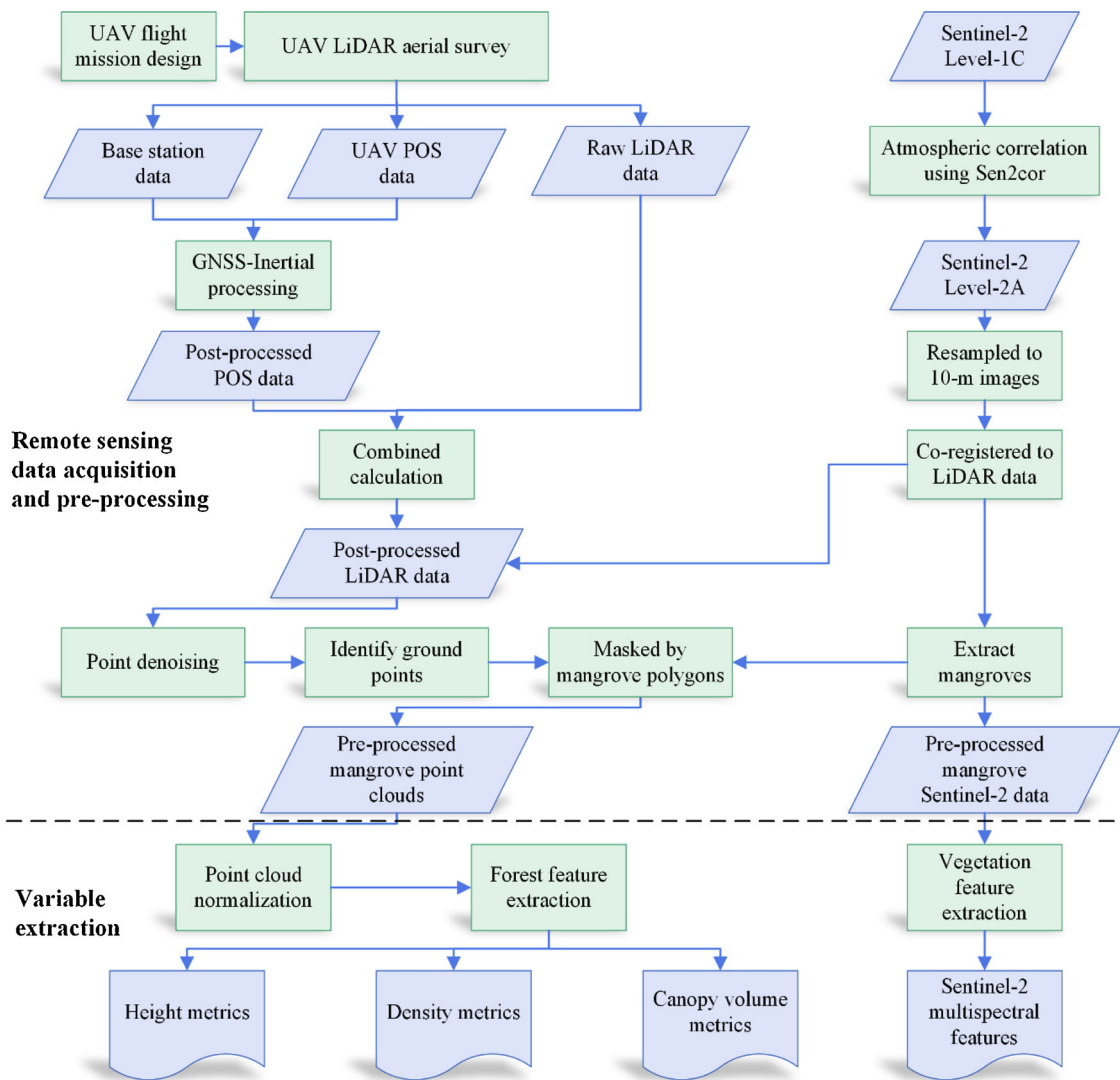


Fig. 3. The workflow of UAV-LiDAR and Sentinel-2 data acquisition and pre-processing and variable extraction.

The Level-1C products were used, which were orthorectified top of atmosphere reflectance data. The images covering the QPR and DNR were acquired on April 8 and 13, 2018, respectively. To generate Level-2A products that were bottom-of-atmosphere reflectance data, the Sen2Cor atmospheric correction processor (version 2.5.5) was used to conduct atmospheric correction. The Sen2Cor processor was developed for formatting and generating Sentinel-2 Level-2A products. The processor is freely available from the European Space Agency website (<http://step.esa.int/main/third-party-plugins-2/sen2cor/>). Then, we resampled the Level-2A images to a 10 m spatial resolution utilizing the nearest neighbor algorithm, while Bands 1, 9, and 10 were discarded because they were dedicated for atmospheric correction and had coarse resolutions of 60 m. Afterwards, the images were co-registered to the LiDAR point clouds with an accuracy of less than 0.5 pixels. Finally, we extracted the mangrove extent according to the method described in Wang et al. (2018a), which employed Sentinel-2 to map the mangrove extent, and produced the post-processed mangrove Sentinel-2 data. The workflow of Sentinel-2 imagery acquisition and pre-processing is shown in Fig. 3.

2.4. Metrics derived from UAV-LiDAR and Sentinel-2 data

Numerous LiDAR derived metrics have been proposed over the past several decades and can be categorized into four groups: height metrics,

density metrics, intensity metrics, and canopy volume metrics (Liu et al., 2018b; Pereira et al., 2018; Shi et al., 2018). The height metrics describe the geometric structures of the trees, such as tree height, and are calculated and derived using height profiles at a given spacing (Dong et al., 2017; Owers et al., 2018). The density metrics delineate canopy return density. The canopy volume metrics directly portray canopy morphology, and these metrics are usually used to assess forest ecosystem functions, such as canopy cover index and leaf area density (Ma et al., 2017). One of the canopy volume metrics, namely, the canopy thickness metric (CTHK), was created in this study based on an analysis of the point clouds of the profile of each mangrove species, which is used to describe the vertical thickness of the mangrove canopy. CTHK is equal to the 90% height percentiles minus the 10% height percentiles, namely H90-H10 (Table 3). The intensity metrics are similar to the height metrics except that they are statistics of the intensity value rather than the height value of the point clouds.

A total of 53 LiDAR metrics were considered for estimating AGB (as listed in Table 3). Because of the low laser pulse energy of the UAV-LiDAR sensor, an intensity banding issue exists. Therefore, we did not use the intensity metrics as predictor variables. Prior to derivation, to eliminate the terrain effect, the mangrove point clouds were normalized, which means that the DEM elevation was subtracted from the height of each LiDAR point. The DEM was derived from the ground points in the LiDAR data. Afterwards, the 53 LiDAR metrics were

Table 3

The list of metrics derived from UAV-LiDAR point clouds.

LiDAR metrics	Formula/Definition
Height metric (24)	Maximum height, Mean height, Median of height Standard deviation of heights, Variance of heights Skewness of heights, Kurtosis of heights Coefficient of variation of height, $(Z_{std}/Z_{mean}) \times 100\%$ Interquartile distance of percentile height, H75th – H25th Height percentiles. Point clouds are sorted according to the elevation. HX is the Xth percentile of height. There are 15 height percentiles metrics from 1% to 99% height.
Density metrics (12)	Canopy return density. Point clouds are divided into slices with the same interval from low to high elevations. DX is the number of canopy return points in the Xth slice compared to the total points. There are 12 density metrics in this study with an interval of 2 m from 0 to 24 m. Canopy cover above 1.3 m, $n_{veg1.3}/n_{total}$. Canopy cover above mean height, $n_{vegmean}/n_{total}$. Canopy relief ratio, $\frac{H_{mean} - H_{min}}{H_{max} - H_{min}}$. Canopy thickness, H90th-H10th.
Canopy volume metrics (17)	Leaf area density. Point clouds are divided into slices with the same interval from low to high elevations. LADX is the valid leaf area density in the Xth slice (Bouvier et al., 2015). There are 11 leaf area density metrics in this study with an interval of 2 m from 2 to 24 m. The scale parameter α and shape parameter β of the Weibull density distribution fitted to the foliage profile (Liu et al., 2018b).

extracted from the normalized point clouds for each field plot. The entire area along the UAV-LiDAR strips was tessellated into a grid of 10×10 m cells with an offset to match the cells of the Sentinel-2 imagery, and the 53 LiDAR metrics were also derived for each cell.

In terms of the Sentinel-2 data, in addition to the 10 original bands, we derived 22 vegetation indices (as listed in Table 4) based on their previous performance in mangroves (Castillo et al., 2017; Wang et al., 2018a; Wicaksone et al., 2016; Zhu et al., 2017) and terrestrial vegetation (Fernandez-Manso et al., 2016; Korhonen et al., 2017; Shoko and Mutanga, 2017) studies.

3. Methods

3.1. AGB upscaling estimation method

Traditionally, field samples were directly related to wall-to-wall

remote sensing data using statistical models for AGB estimation (Fig. 4A). The most popular auxiliary data are satellite images and airborne laser scanning (ALS) data. By summarizing airborne and spaceborne LiDAR sampling and digital stereo imagery sampling for terrestrial forests (Huang et al., 2019; Nelson et al., 2017; Puliti et al., 2018) and inspired by various mobile techniques such as backpack LiDAR, UAV-LiDAR, mobile car LiDAR (Guo et al., 2017; Polewski et al., 2019), we defined a point-line-polygon framework to generalize all methods that employ linear-remotely sensed data as intermediate data for AGB estimation (Fig. 4B).

The point data, named G, denote ground measurements from field plots, such as AGB measurements from destructive harvesting techniques or field estimated AGB derived from tree height, DBH and allometric equations. The points should be well spatially distributed and account for potential variations in AGB. The line data, named L, denote remotely sensed data that are produced by mobile measurement

Table 4

The list of indices derived from Sentinel-2 data.

Sentinel-2 Feature	Formula/Definition	Reference	
Spectral bands (10)	individual bands	NA	
Conventional near infrared indices (8)	B2, B3, B4, B5, B6, B7, B8, B8a, B11, B12 (B8/B3) - 1 B8 - B4 $\frac{2.5 \times (B8 - B4)}{B8 + 6 \times B4 - 7.5 \times B2 + 1}$ B8-(B3 + B4) (B3-B11)/(B3 + B11) (B8-B4)/(B8 + B4) B8/B4 $\sqrt{[(B8 - B4)/(B8 + B4) + 0.5]}$	(Gitelson et al., 2003) (Zhu et al., 2015) (Huete et al., 2002) (Kamal et al., 2015) (Ji et al., 2009) (Valderrama-Landeros et al., 2018) (Wicaksone et al., 2016) (Castillo et al., 2017)	
Red edge indices (12)	Clg-re1 Clg-re2 Clg-re3 IRECI MTCI MCARI MSRren NDVIre1 NDVIre2 NDVIre3 PSSRa S2REP	B5/B3-1 B6/B3-1 B7/B3-1 (B7-B4)/(B5/B6) (B6-B5)/(B5-B4) [(B5-B4)-0.2 × (B5-B3)] × (B5/B4) $\frac{(B8a / B5) - 1}{\sqrt{(B8a / B5) + 1}}$ (B8-B5)/(B8 + B5) (B8-B6)/(B8 + B6) (B8-B7)/(B8 + B7) B7/B4 705 + 35 × [(B4 + B7)/2-B5]/(B6-B5)	(Gitelson et al., 2003) (Gitelson et al., 2003) (Gitelson et al., 2003) (Castillo et al., 2017) (Dash and Curran, 2004) (Daughtry et al., 2000) (Fernandez-Manso et al., 2016) (Shoko and Mutanga, 2017) (Shoko and Mutanga, 2017) (Shoko and Mutanga, 2017) (Blackburn, 1998) (Frampton et al., 2013)
Shortwave infrared indices (2)	MDI1 MDI2	(B8-B11)/B11 (B8-B12)/B12	(Wang et al., 2018a) (Wang et al., 2018a)

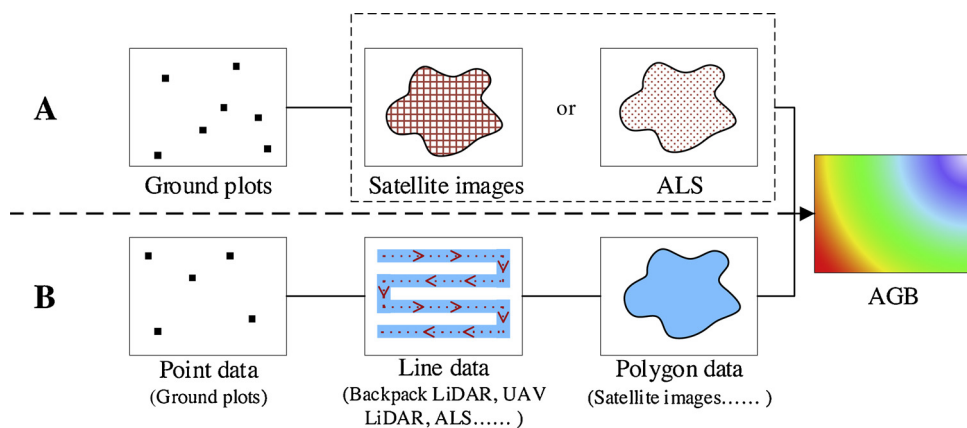


Fig. 4. A schematic graph of traditional (A) and point-line-polygon (B) frameworks for AGB estimation.

systems, which usually have high resolution and can capture vertically distributed attributes of forests. Therefore, the line data can provide accurate AGB estimates and serve as sampling tools for measuring forest AGB. The polygon data, name P, represent large-scale, full coverage and relatively low-resolution remote sensing imagery, for example, MODIS, Landsat TM/ETM and SPOT images. These data are usually less sensitive to forest vertical structure but are free or available at low cost. In this framework, the point coverage AGB measurement (set G) is first extrapolated to line coverage. The line AGB estimates (set L) are subsequently sampled and used as reference data for polygon coverage (set P) to generate the AGB.

Based on the point-line-polygon framework, we proposed a mangrove AGB upscaling method by integrating field plots, UAV-LiDAR strip data and Sentinel-2 imagery, namely, the $G \sim \text{LiDAR} \sim S2$ model. Using UAV-LiDAR data as a linear bridge, field plots were first linked with the corresponding UAV-LiDAR plots by a random forest model $G \sim \text{LiDAR}$, and then this model $G \sim \text{LiDAR}$ was extrapolated to all UAV-LiDAR grid cells (Eq. 1, Fig. 5).

$$\text{AGB}_{G \sim \text{LiDAR}} = f_{RF}(x_{\text{UAVLiDAR}}) \quad (1)$$

where $\text{AGB}_{G \sim \text{LiDAR}}$ denotes the predicted AGB using ground measurements and UAV-LiDAR data, f_{RF} denotes a random forest function, and x_{UAVLiDAR} denotes the matrix of the selected UAV-LiDAR predictor variables.

Subsequently, the UAV-LiDAR transects were used as a linear bridge to transfer the ground measurements to full coverage Sentinel-2 imagery. Specifically, the $\text{AGB}_{G \sim \text{LiDAR}}$ data of all LiDAR grid cells were used as reference data, and then the Sentinel-2 data together with a random

forest model, $\text{UAVLiDAR} \sim S2$, were utilized to estimate the AGB for all study areas (Eq. 2). In other words, the AGB prediction from the UAV-LiDAR data was modeled as a function of Sentinel-2 predictor variables (Fig. 5).

$$\text{AGB}_{\text{UAVLiDAR} \sim S2} = f_{RF}(x_{S2}) \quad (2)$$

where $\text{AGB}_{\text{UAVLiDAR} \sim S2}$ denotes the estimated AGB based on the UAV-LiDAR-predicted AGB from model (1) and auxiliary Sentinel-2 data, and x_{S2} denotes the matrix of selected Sentinel-2 predictor variables. The $G \sim \text{LiDAR}$ and $\text{UAVLiDAR} \sim S2$ together form an instance of a “point-line-polygon” framework and are named as $G \sim \text{LiDAR} \sim S2$.

For method comparison, a traditional model was also constructed using only field plots and Sentinel-2 imagery, which was used as a benchmark in the paper. A random forest regression model $G \sim S2$ was first developed, and then the AGB of whole mangrove forests could be directly extrapolated from the ground measurements (Eq. 3).

$$\text{AGB}_{G \sim S2} = f_{RF}(x_{S2}) \quad (3)$$

where $\text{AGB}_{G \sim S2}$ is the predicted AGB using ground measurements and Sentinel-2 data, and x_{S2} is the matrix of selected Sentinel-2 predictor variables.

In this study, we used only the LiDAR grid cells ($10 \times 10 \text{ m}$) that were 20 m away from the flight strip centerlines, and the other LiDAR data were discarded. This procedure was employed because the point cloud density in this 40 m range is more uniform. We first implemented the $G \sim \text{LiDAR} \sim S2$ model in the QPR using 69 field samples (45 in the LiDAR area) and 10988 UAV-LiDAR grid cells to examine the effectiveness of the model at the local scale (Table 5). Subsequently, the 28

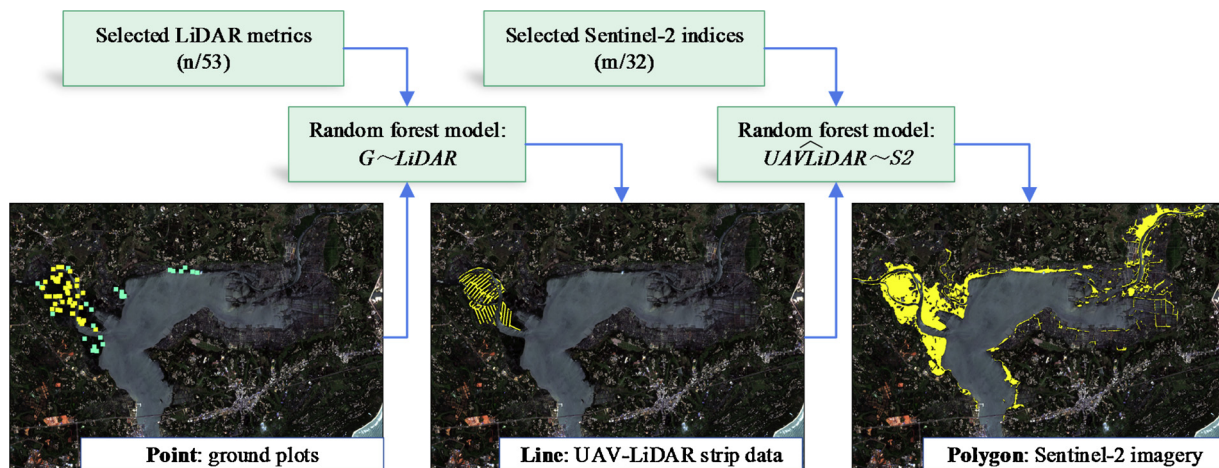


Fig. 5. An example of the point-line-polygon framework using ground plots, UAV-LiDAR strip data and Sentinel-2 imagery for mangrove AGB upscaling estimation on a local scale (the QPR).

Table 5

Summary of the models, training samples, and validation samples used in the point-line-polygon framework for local and regional scale mangrove AGB extrapolations.

Scale	Stage	Model	Training sample	Validation sample
Local scale	point-line	G~LiDAR	45 field samples	10-fold cross-validation
	line-polygon	UAVLiDAR ~ S2	10988 LiDAR plots	24 field samples
Regional scale	point-line	G~LiDAR	62 field samples	10-fold cross-validation
	line-polygon	UAVLiDAR ~ S2	14628 LiDAR plots	35 field samples

field samples (all in the LiDAR area) and 3640 UAV-LiDAR grid cells from the DNR were added to the QPR dataset and computed again to assess the effectiveness of the G~LiDAR~S2 model at the regional scale, namely over northeast Hainan Island. In the intermediate point-line stage, the 10-fold cross-validation approach that was run 10 times was used to evaluate the accuracy of the G~LiDAR model. The accuracy of the line-polygon stage also stands for the final AGB estimation accuracy of the G~LiDAR~S2 model. Table 5 presents the specific models and samples implemented in this study.

3.2. UAV-LiDAR linear bridge for reducing field samples

One of the objectives of the study was to examine whether the use of UAV-LiDAR as a linear bridge could reduce the number of necessary field samples required to estimate mangrove AGB without the loss of accuracy. This objective was addressed by comparing the accuracy of AGB estimates derived from the G~LiDAR~S2 model with the accuracy of the AGB prediction by the traditional approach G~S2 model at the regional scale. The number of field plots was iteratively increased by 5 plots (the maximum number of field samples that can be measured by a team of 3 or 4-people in a half day in mangrove forests) at a time for the G~S2 model until all ground plots (97) were input. Before adding plots, the 35 field samples that were used as validation samples in section 3.1 at the regional scale were first sorted by increasing values of AGB and then divided into 5 strata of seven consecutive observations. Subsequently, one out of seven observations per stratum was randomly selected to compile a group of 5 plots. This random selection process was repeated 100 times and the new subset was used to predict AGB. The performances of the 100 times were recorded and averaged. Since the validation plots were gradually added to the G~S2 model, there were not enough observations to validate the model performance with an independent subset. Therefore, a 10-fold cross-validation method was employed and repeated 10 times as suggested by Ghosh and Behera (2018). The same 10-fold cross-validation process that was iterated 10 times was also applied to the G~LiDAR~S2 model to obtain cross-validation accuracy.

3.3. The effect of UAV-LiDAR sampling intensity

The sampling intensity of UAV-LiDAR not only controls the number of UAV-LiDAR plots but also influences the cost of UAV-LiDAR data collection. Therefore, when the distribution and structure of mangroves in a study area are roughly known, the number of representative mangrove samples that should be collected and covered is our major concern. Furthermore, whether the sampling intensity of UAV-LiDAR influences the accuracy of mangrove AGB estimates also requires investigation.

In the case of the previously obtained typical and representative mangrove point clouds in the QPR and DNR, we adopted a subsampling method (from 100% to 10% of the original LiDAR plots, namely, from 14628 to 1463, and randomly eliminated 10% samples at a time) to investigate the influence of the UAV-LiDAR sampling intensity. The first stage G~LiDAR model was the same, but the numbers of LiDAR plots involved in building the UAVLiDAR ~ S2 model were different. The 10% random elimination process was iterated 100 times, and the

resultant average accuracies were obtained. The accuracies were still evaluated by the 35 independent ground measurements, as described in section 3.1.

3.4. Random forest algorithm and variable selection

The above used random forest (RF) regression is a popular and powerful ensemble machine learning algorithm that creates a large collection of decision trees and provided prediction results by averaging the predictions of all regression trees (Breiman, 2001; Pham and Brabyn, 2017; Shao et al., 2019). When creating a user-defined number of trees (*ntree*), the corresponding number of training sample subsets are drawn from the original training dataset through the replacement method (namely, bagging), and the subsets are used to construct the regression trees. The size of these subsets is the same as the original training dataset. During the growth of the trees, a user-defined number of variables (*mtry*) are randomly selected from all variables and utilized to determine the best split at each node. The individual tree of a random forest has high variance and low bias (Breiman, 2001). However, when the number of trees is sufficiently large, the variance of ensemble trees decreases significantly, and the bias remains mostly unchanged (Breiman, 2001). Therefore, RF has been widely used in biomass estimations (Ghosh and Behera, 2018; Huang et al., 2019; Matasci et al., 2018; Pham and Brabyn, 2017). When building RF models in this study, the value of *ntrie* was set as 5000, and the *mtry* parameter was set as the default value $\sqrt{n_{mtry}}$ (n is the total number of input predictor variables).

A variable selection process was also conducted via the backward feature elimination method prior to the final estimation due to the large number of Sentinel-2 (32) and UAV-LiDAR variables (53) input. As usual, a model constructed from a small number of variables is more interpretable, and eliminating irrelevant and highly correlated variables may improve the predictive power (Gregorutti et al., 2017). The backward feature elimination approach is based on the random forest algorithm and compares the cross-validated prediction results of models as a proportion of the predictors is eliminated. This method was implemented by the rfcv function in the randomForest package and replicated 100 times with 5-fold cross-validation to get the optimal variables (Pham and Brabyn, 2017). Table 6 summarizes the optimal variables for each model at local and regional scales.

3.5. Accuracy assessment

The final accuracy of the AGB estimates was assessed using independent validation samples by comparing the predicted to observed values using the coefficient of determination R^2 , root mean square error (RMSE) and RMSE expressed as a percentage of the observed mean (RMSE%) (Matasci et al., 2018; Pham and Brabyn, 2017). The final AGB estimation accuracies of the G~LiDAR~S2 and G~S2 models were assessed by 24 and 35 independent field samples for local and regional scales, respectively (Table 5). The former 24 field plots were outside the LiDAR data area in the QPR. At the regional scale, the 35 independent samples were compiled from the 24 field samples of the local scale and the 11 randomly selected field samples that were collected in advance from the DNR.

Table 6

Summary of the selected predictor variables for each model at local and regional scales in the study.

Scale	Model	Number	Predictor variables
Local	G~S2	11	B11, B2, MNDWI, B12, Clre1, MDI1, B3, B4, MDI2, B5, Clre2
	G~LiDAR	12	CTHK, HIQ, H80, HVAR, HSD, D06, H95, H90, LAD11, H75, CC _{1,3} , H01
	UAVLiDAR ~ S2	10	B11, B12, B5, S2REP, MNDWI, NDVire3, MTCl, MCARI, NDVire2, B2
Regional	G~S2	14	B5, B2, B3, MNDWI, MDI1, EVI, B4, Clre1, NDVire2, NDVire1, SR, MTCl, B11, Clre3
	G~LiDAR	11	CTHK, HIQ, HVAR, H05, H80, HSD, H95, H90, D01, CC _{1,3} , H10
	UAVLiDAR ~ S2	12	B11, B12, S2REP, NDVire3, MTCl, MDI1, MDI2, NDVire2, MCARI, B2, MNDWI, B7

Table 7

Calibration and validation results of the AGB models at local and regional scales.

Framework	Scale	Model	Calibration		Validation	
			R ²	RMSE (%)	R ²	RMSE (%)
Point-line-polygon	Local scale	G~LiDAR	0.67	47.78 (27.15%)	0.65	49.40 (28.07%)
		UAVLiDAR ~ S2	0.50	46.31 (26.32%)	0.35	47.84 (25.94%)
	Regional scale	G~LiDAR	0.80	40.54 (28.13%)	0.78	42.29 (29.35%)
		UAVLiDAR ~ S2	0.67	41.29 (28.65%)	0.62	50.36 (35.41%)
Traditional	Local scale	G~S2	0.28	70.61 (40.13%)	0.12	55.51 (30.10%)
	Regional scale	G~S2	0.48	64.92 (45.05%)	0.52	56.63 (39.82%)

4. Results

4.1. Accuracy comparison

Table 7 summarizes the results of the calibration and validation for each of the three models at two different scales. The final predicted AGB values from the proposed G~LiDAR~S2 model and the traditional G~S2 model versus the field estimated AGB at the two scales are plotted in **Fig. 6**. In the QPR, the G~LiDAR~S2 model performed moderately but better than the G~S2 model (R^2 : 0.35 > 0.12, RMSE: 47.85 Mg ha⁻¹ < 55.51 Mg ha⁻¹). When extended to the regional scale, i.e., the entire northeast of Hainan Island, the proposed G~LiDAR~S2 model was also superior to the conventional G~S2 model (R^2 : 0.62 > 0.52, RMSE: 50.36 Mg ha⁻¹ < 56.63 Mg ha⁻¹). In addition, **Fig. 6** indicates that both the G~LiDAR~S2 and G~S2 models overestimated low AGB and underestimated high AGB. For medium AGB ranging from 100 to 250 Mg ha⁻¹, which is the main range of mangrove AGB in this region, the G~LiDAR~S2 model demonstrated greater explanatory power compared to the G~S2 models, with points scattered closer to the 1:1 line.

4.2. The mangrove AGB of northeast Hainan Island

The final mangrove AGB map of northeast Hainan Island derived from the regional G~LiDAR~S2 model using RF regression is presented in **Fig. 7**. The detailed mangrove AGB values are shown in **Table 8**. **Fig. 7** portrays that the mangroves of northeast Hainan Island are located in four places, namely, the DNR, Qinglan Harbor, Puqian, and Fengjia Harbor. The latter three constitute the QPR. The total mangrove AGB of northeast Hainan Island was 312,806.29 Mg with a mean AGB of 119.26 Mg ha⁻¹. The DNR had a higher total mangrove AGB covering 1508.14 ha, while the QPR had a greater mangrove AGB density with a value of 136.57 Mg ha⁻¹. In the DNR, the mangrove AGB in the north was visually lower than that in the south (**Fig. 7B**). For the Qinglan Harbor, namely, the core area of the QPR, its mangrove AGB density was highest among the four sites, and the AGB distribution was relatively even with the small AGB values only lying in several local areas (green color in **Fig. 7C**). Regarding the mangroves in Puqian Harbor and Fengjia Harbor, the AGB was relatively low, with a mean value of approximately 60 Mg ha⁻¹.

4.3. The effectiveness of reducing field samples

The results of the comparison between the G~LiDAR~S2 model that used a constant sample size of 62 field plots and the G~S2 model that employed varying field sample sizes are presented in **Table 9**. The approach for simulating an increase in the field sample size of the G~S2 model based on a stratified random selection without replacement produced a continuous curve, as presented in **Fig. 8**. The results showed that when the number of field plots increased, the AGB estimation accuracy exhibited an increasing trend for the G~S2 model. Specifically, as the number of field samples increased from 62 to 97, the R^2 increased from 0.4331 to 0.5059 and the RMSE% decreased from 47.06% to 42.82%, which was still lower than the accuracy of the G~LiDAR~S2 mode that used 62 ground observations (R^2 = 0.5514 and RMSE% = 41.87%).

As delineated in **Fig. 8**, the trends of the R^2 and RMSE% values in varying field sample sizes could both be fitted by linear regression equations with high R^2 values. Due to the different training sample sizes, only the RMSE% was used to extrapolate how many field plots were required by the traditional G~S2 model to achieve the accuracy of the proposed G~LiDAR~S2 approach that utilized 62 field plots. As calculated from the equation $y = -0.0013x + 0.5489$ ($R^2 = 0.9728$) derived from **Fig. 8**, when the number of field plots (x) increases to 101, the RMSE% (y) of the G~S2 model will be equal to the RMSE% of the G~LiDAR~S2 model using 62 ground samples. This implies that the G~LiDAR~S2 model requires approximately 39% fewer field samples compared to the traditional G~S2 model in the study area.

4.4. The influence of UAV-LiDAR sampling intensity

Fig. 9 indicates that when the number of LiDAR plots decreased by 10% at a time, there is an overall decreasing trend in the estimated accuracies, especially from 20% (2926 plots) to 10% (1463 plots) sampling intensities. However, compared with the original LiDAR sampling intensity, the accuracy produced by 20% of the original LiDAR samples did not drastically decrease with the R^2 and RMSE decreasing by less than 0.01 and 1 Mg ha⁻¹, respectively.

5. Discussion

The estimation of AGB over large areas in mangrove forests is

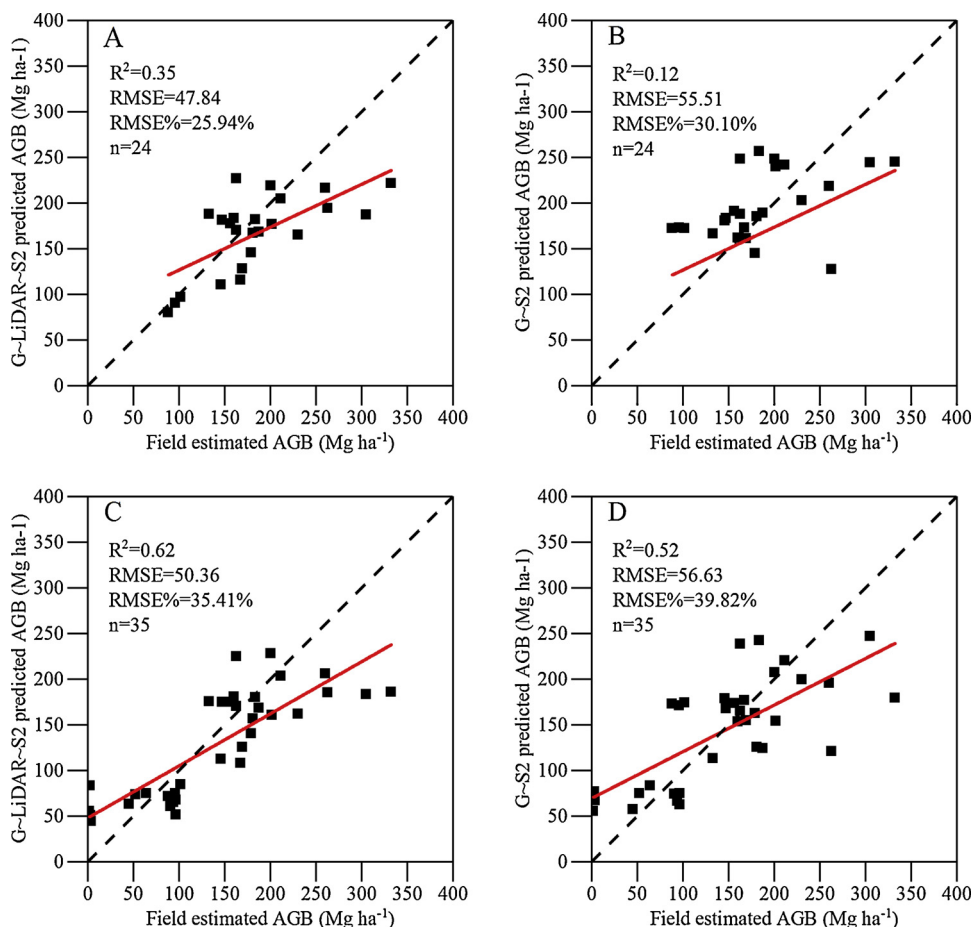


Fig. 6. The scatterplots of field estimated and model predicted AGB. A: G~LiDAR~S2 model at the local scale; B: G~S2 model at the local scale; C: G~LiDAR~S2 model at the regional scale; D: G~S2 model at the regional scale.

challenging. As the most species diverse and important mangrove forests in China, the mangroves of northeast Hainan Island remain poorly studied. Until now, no mangrove biomass map has been presented for this region. This study presents the first mangrove AGB map of northeast Hainan Island. This map was achieved by proposing a novel AGB upscaling method (G~LiDAR~S2 model) that integrated field plots, UAV-LiDAR data and Sentinel-2 imagery.

5.1. The feasibility of the mangrove AGB upscaling method

Large-scale mangrove AGB estimations are usually limited by the difficulty in acquiring enough field measurements because mangroves grow in harsh environments that are hard to access. Most mangrove AGB estimation studies are conducted over small areas or at a local scale (Jachowski et al., 2013; Pereira et al., 2018) and are limited to a small number of field samples (the number of plots is usually < 50). In this study, the proposed G~LiDAR~S2 model enables mangrove AGB upscaling without the need for extensive field measurements. In particular, we demonstrated the effectiveness of using UAV-LiDAR to act as a more flexible tool to link field plots with Sentinel-2 data. The results turned out to be quite promising, even in the highly diverse mangrove forests on Hainan Island.

The proposed G~LiDAR~S2 model performed moderately well in terms of calibration accuracy (also called model fit accuracy, $R^2 = 0.50$ and RMSE% = 26.32%) and validation accuracy (also referred to AGB map accuracy, $R^2 = 0.35$ and RMSE% = 25.94%) in the QPR. However, when extending the study from the local scale to the regional scale, namely, from the QPR to northeast Hainan Island, by adding the point, line, and polygon data of the QPR, the accuracies were improved to an

R^2 of 0.62 and RMSE% of 35.41%. There are two likely reasons for the improvement. The first is that the increasing field sample and LiDAR plot size may fit a more explanatory model (Liu et al., 2018b; Puliti et al., 2018). The mangrove species in the DNR field plots are mainly *R. stylosa*, *C. tagal* and *A. marina*, which have relatively low biomass and they have different structures in comparison with those in the QPR. The combination of the field plots and LiDAR sampling data from the two reserves could cover more of variations in mangrove forest biomass in this region. This condition also explains why there were different selected predictor variables at the local and regional scales, as presented in Table 6. Second, because the biodiversity and structural variation in the DNR are lower than those in the QPR, the difficulty of fitting the model may be reduced when integrating the QPR with the DNR. Accordingly, the model predictive power would be improved. For example, as shown in Fig. 6C, the AGB values lower than 100 Mg ha^{-1} (mainly from the DNR) are well predicted, and the AGB values higher than 100 Mg ha^{-1} are closer to the 1:1 line than those shown in Fig. 6A. Therefore, using UAV-LiDAR and Sentinel-2 data to construct a mangrove AGB upscaling method based on the point-line-polygon framework is feasible. Furthermore, at both the local and regional scales, the accuracies of the G~LiDAR~S2 model were higher than those of the G~S2 model. These findings prove the superiority of the upscaling method compared with the traditional approach. This result is consistent with the results of previous studies by Nelson et al. (2017) and Matasci et al. (2018), who also used airborne LiDAR data as sampling tools. The theoretical reason for this result is that using the linear bridge as a sampling tool could capture a wider range of possible vegetation vertical and horizontal structure variations as well as measuring terrain morphology in detail and with high accuracy. Then, when these large-

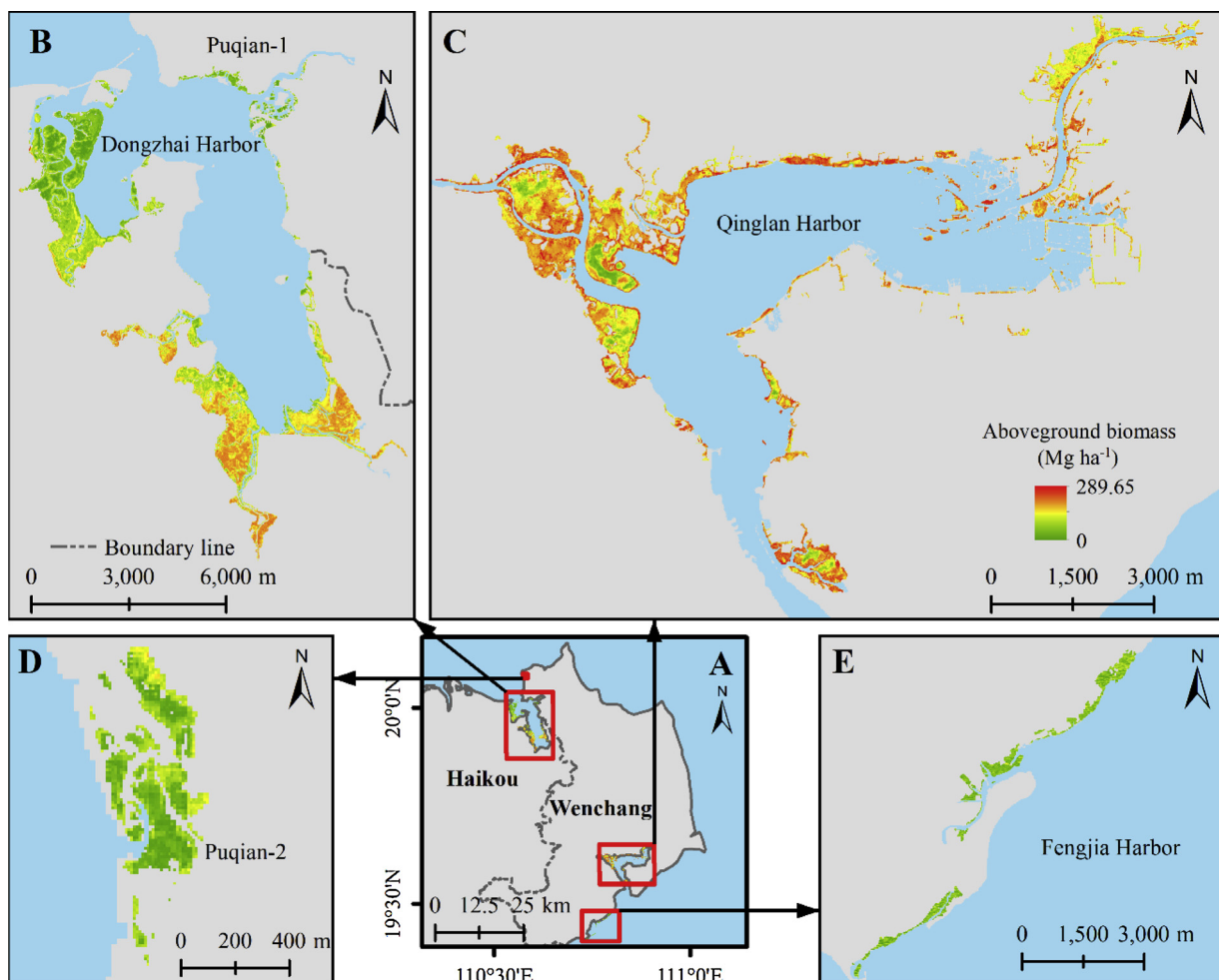


Fig. 7. Mangrove aboveground biomass map of northeast Hainan Island at 10 m spatial resolution (A). The mangrove forests of this region are located in four areas, namely, the DNR (B), Qinglan Harbor (C), Pujian (D), and Fengjia Harbor (E). The latter three constitute the QPR. Some of the mangroves in Pujian are distributed in Fig. 7B, namely, north of the boundary line, and are called Pujian-1.

Table 8
Summaries of the mangrove aboveground biomass of northeast Hainan Island.

Location	Area (ha)	Total mangrove AGB (Mg)	Mean AGB ($Mg\ ha^{-1}$)	Standard deviation ($Mg\ ha^{-1}$)
DNR QPR	1508.14	160,565.38	106.47	45.22
	888.71	138,609.70	155.97	39.66
	88.48	5469.53	61.82	26.79
	137.52	8161.68	59.35	22.41
	Sum	1114.71	152,240.91	136.57
	Northeast Hainan Island	2622.85	312,806.29	119.26
				53.40
				51.08

coverage and accurate AGB estimates that are derived from the linear bridge data are used as training samples, the model can cover and fit as many variations and relationships as possible between biomass and variables and produce a high prediction accuracy.

Compared with other mangrove AGB retrieval studies, the accuracy of the regional GLiDAR-S2 model ($R^2 = 0.62$ and RMSE% = 35.41%) was similar to the accuracy reported by Jachowski et al. (2013) based on GeoEye-1 imagery with 2 m spatial resolution ($R^2 = 0.66$, RMSE % = 23.60%), slightly higher than that reported by Pham and Brabyn (2017) based on SPOT-5 imagery with 10-m spatial resolution ($R^2 = 0.52$ -0.63, RMSE% = 40%) and higher than the accuracy reported by Asian et al. (2016) using SRTM data ($R^2 = 0.55$, RMSE % = 47.07%), but lower than the accuracy reported by Castillo et al. (2017) based on Sentinel-2 and Sentinel-1 imagery ($R^2 = 0.83$, RMSE% = ~40%). A possible explanation for the accuracy in this study lower than the accuracy reported by Castillo et al. (2017) may be that the mangrove forests investigated in their study were simple and

Table 9

Average results of the G-S2 model and the G-LiDAR-S2 model over 100 times of random selection using 10-fold cross-validation for each number of field plots.

Model	G-LiDAR-S2	G-S2							
Field samples	62	62	67	72	77	82	87	92	97
R^2	0.5514	0.4331	0.4334	0.4566	0.4747	0.4757	0.4853	0.5022	0.5059
RMSE	60.33	67.81	67.36	65.73	63.81	63.91	62.93	62.02	61.40
RMSE%	41.87%	47.06%	46.82%	45.62%	44.67%	44.57%	43.80%	43.24%	42.82%

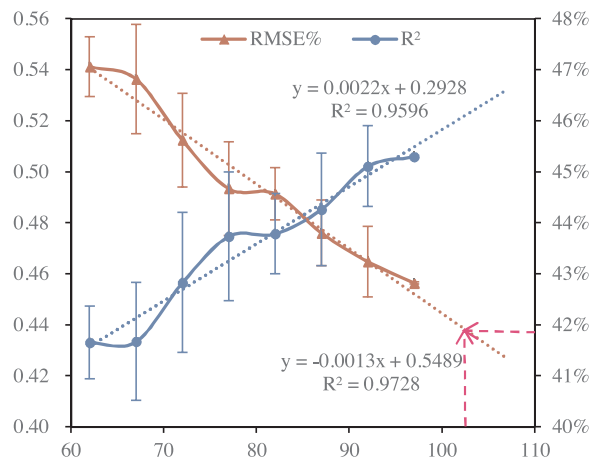


Fig. 8. The variation trends of R^2 and RMSE% of the G~S2 model in varying numbers of ground plots.

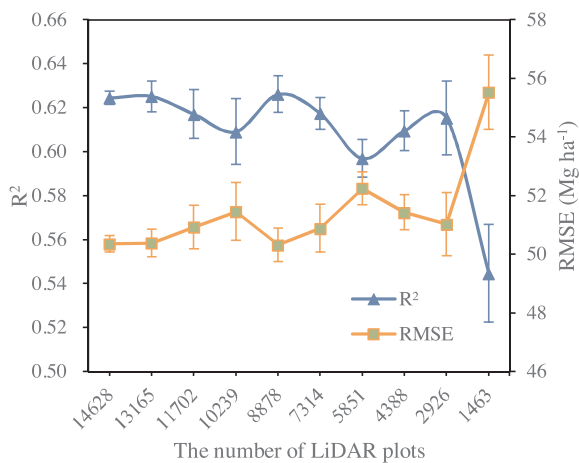


Fig. 9. The variation trends of the average R^2 and RMSE% values with the decrease in the UAV-LiDAR linear bridge size.

dominated mostly by one genus, *Rhizophora*. Considering our study was carried out in a mangrove forest with a complex structure and abundant species, the resultant accuracy is inspiring. The results of the traditional G~S2 model (model fit accuracy: $R^2 = 0.28$ and RMSE% = 40.13%; and test accuracy: $R^2 = 0.12$ and RMSE% = 30.10%) were lower than the usual precision of mangrove AGB estimates ($R^2 > 0.6$ and RMSE % < 35%) (Castillo et al., 2017; Pham and Brabyn, 2017; Zhu et al., 2015), which might also imply that the model was difficult to fit in the study area (Fig. 6). Overall, the proposed upscaling method could produce satisfactory results for AGB estimations over large areas of highly diverse mangroves without extensive field measurements.

The point-line-polygon framework is the basis of the mangrove AGB upscaling method. This framework generalizes previous studies that used airborne and spaceborne LiDAR and digital stereo imagery as sampling tools and absorbs the more mobile and flexible advantages of UAV-LiDAR. This framework provides a common flow for forest AGB estimation when employing intermediate remotely sensed data as a linear bridge. For example, in the future, we could use backpack LiDAR to capture tree stem and understory plant information and employ this transect as a linear bridge for dense forest AGB assessments.

5.2. The AGB of the mangrove forests on northeast Hainan Island

This study estimated that the total mangrove AGB of northeast Hainan Island was 312,806.29 Mg with a mean AGB of 119.26 Mg ha^{-1} , which is higher than the mangrove AGB density reported in other

locations in China, such as the Jiulong River Estuary, Fujian, China ($79 \text{ Mg } ha^{-1}$) (Wang et al., 2018b) and Shenzhen Bay, Guangdong, China ($54.81 \text{ Mg } ha^{-1}$) (Jiang et al., 2018). Compared with other countries, the average AGB of the mangrove forests in northeast Hainan Island, China ($119.26 \text{ Mg } ha^{-1}$), was similar to the AGB of the Cangio mangrove forest in Vietnam ($119\text{--}130 \text{ Mg } ha^{-1}$) reported by Pham and Brabyn (2017), also similar to the mangrove AGB in Africa ($116 \text{ Mg } ha^{-1}$) reported by Fatoyinbo and Simard (2013), greater than the AGB of a mangrove forest in northwest Australia ($70 \text{ Mg } ha^{-1}$) reported by Hickey et al. (2018), but lower than the mangrove AGB of Papua, Indonesia ($292.72 \text{ Mg } ha^{-1}$) reported by (Asian et al., 2016). The Cangio mangrove forests had various mangrove species and were recognized as the first biosphere reserve in Vietnam (Pham and Brabyn, 2017). The reason why the mangrove AGB density of northeast Hainan Island is lower than that of Papua, Indonesia is that the mangroves of Papua are closer to the equator and have high biodiversity and complex structures with approximately 40% mixed mangrove forests and a mean canopy height of 20.8 m. Although the mangrove forests on northeast Hainan Island have abundant species, their mean canopy height is only 6.8 m. Simard et al. (2006) and Simard et al. (2008) showed that the mangrove AGB is directly related to the canopy height. Saenger and Snedaker (1993) provided a global stand height to biomass allometric equation for mangrove forests— $AGB (\text{Mg } ha^{-1}) = 10.8 \times H(\text{m}) + 35$.

The mean mangrove AGB of northeast Hainan Island is nearly double the average forest AGB of China ($61.8\text{--}73.4 \text{ Mg } ha^{-1}$) (Huang et al., 2019) and accounts for approximately 65% of the global mangrove AGB density ($184.8 \text{ Mg } ha^{-1}$) (Hutchison et al., 2014). There is no specific national mangrove AGB density in China reported to date.

Consequently, the average mangrove AGB of northeast Hainan Island is higher than that in other places in China, but lower than the global average value. This mangrove AGB value could serve as a reference value for future studies on biomass changes or mangroves' responses to global warming and sea level rise.

5.3. UAV-LiDAR data and Sentinel-2 imagery

The UAV-LiDAR data play a vital role in building the G~LiDAR~S2 model for mangrove AGB estimation. The flexibility, low-cost and high point density are the major advantages of UAV-LiDAR, in comparison with airborne and spaceborne LiDAR used in previous research (Nelson et al., 2017). First, as a new emerging and low-cost active remote sensing technology, UAV-LiDAR can characterize the vertical structure of forest ecosystems at fine spatial resolution (Guo et al., 2017). In this study, the average UAV-LiDAR point density was 94 points/ m^2 , which was significantly higher than that of airborne LiDAR (usually < 25 point/ m^2) (Liu et al., 2018b). In general, the higher the point density is, the finer the tree canopy that will be detected, and the bottom terrain will be detected more easily. For example, previous studies used only canopy height information to estimate mangrove AGB when using ALS data due to sparse point clouds (Asian et al., 2016; Simard et al., 2006). In contrast, with dense UAV-LiDAR point clouds, we could detect much more detailed canopy structures, including height (such as H01, H10, H80, H90, H95), canopy thickness (such as CTHK) and canopy cover (such as CC_{1,3}), to predict mangrove AGB (Table 6). Fig. 10 presents the vertical and horizontal pictures of *B. sexangula* and *R. stylosa* based on UAV-LiDAR data in the study area. Therefore, in the point-line stage of this study, the UAV-LiDAR data could adequately derive mangrove AGB at the local scale ($R^2 = 0.65$, RMSE% = 28.07%) and resulted in high accuracy at the regional scale ($R^2 = 0.78$, RMSE% = 29.35%). Second, UAV-LiDAR has higher flexibility than airborne and spaceborne LiDAR (Yin and Wang, 2019) and is suitable for forest inventories. As an intertidal forest spread over coasts with low wave energy, mangroves usually appear as more elongated and dispersed patches than terrestrial forests (Wang et al., 2019), such as the mangroves in the QPR (Figs. 1 and 7). The lightweight and easily operational UAV-LiDAR can efficiently collect

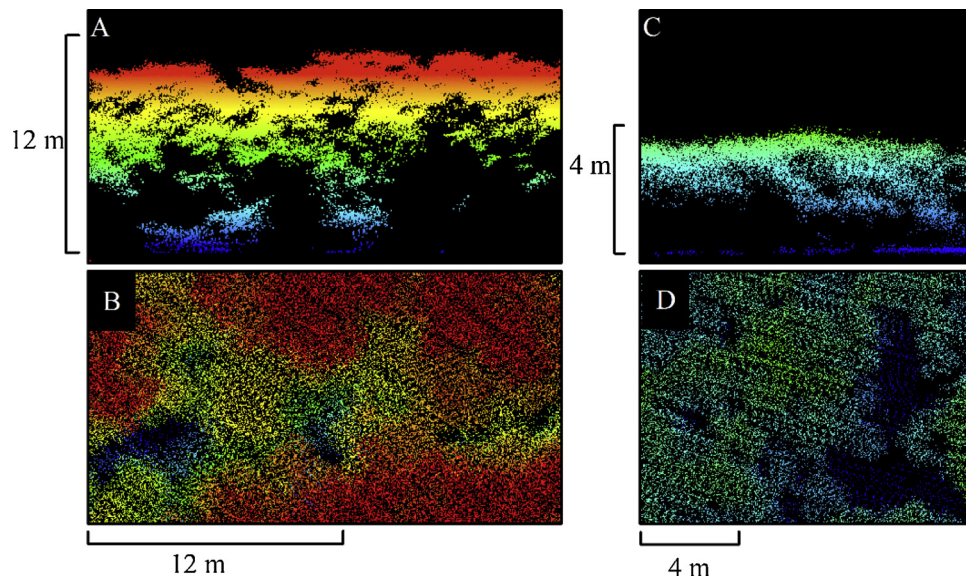


Fig. 10. The vertical and horizontal pictures of *B. sexangula* (A and B) and *R. stylosa* (C and D) based on UAV-LiDAR data.

mangrove data on any low-wind day with arbitrary time intervals.

Although UAV-LiDAR has the abovementioned advantages, it also has several drawbacks. First, the UAV-LiDAR could scan only a small area of forests in one flight (usually < 50 ha). In this study, we obtained an average of 28 ha/flight. This is also one of the reasons why we used UAV-LiDAR as a linear bridge and not as wall-to-wall data. Second, the laser sensor mounted on UAV has a short detection range and weak penetration capability in comparison with airborne laser sensors, which means that UAV-LiDAR may have difficulty in capturing the middle branches, understory plants and bottom prop roots of mangroves. Third, due to the intensity banding issue (Yan and Shaker, 2018), the intensity metrics are difficult to use as valid predictor variables. The problem may be caused by the low laser pulse energy of the UAV-LiDAR sensor, which leads to apparent power attenuation in the travel distance for laser beams. In the future, if we design a non-overlapping flight route and use only the LiDAR points within a very small distance of the central strip as sampling plots, the intensity banding issue may be overcome.

The proposed G~LiDAR-S2 model also benefits greatly from the Sentinel-2 imagery. First, the Sentinel-2 imagery is unique freely- and globally-available data at 10 m spatial resolution. More than 90% of the world's mangroves are located in developing countries (Duke et al., 2007), which may have limited funding for purchasing large area commercial satellite imagery. The freely- and globally-available Sentinel-2 imagery has become an excellent remote sensing data for mangrove inventories, either at local scale or regional scale (Castillo et al., 2017; Wang et al., 2018a). Second, the Sentinel-2 imagery has three red-edge bands. The spectral reflectance curve of plants usually rises rapidly in the red edge (central wavelength: 0.68~0.78 μm) and this slope is highly correlated with the chlorophyll content per area (Horler et al., 1983). So, the Sentinel-2 imagery provides a new opportunity for mangrove biomass estimation. In this study, approximately half of the selected predictor variables are from red-edge bands and their derived indices, such as Band5, CIre1, S2REP and NDVIre3 (Table 6). This result is consistent with previous research, which found red-edge vegetation indices are highly correlated with biomass even in dense vegetation canopies (Mutanga and Skidmore, 2004). Third, the Sentinel-2 has a short revisit period of 5 days due to its double satellite system (Drusch et al., 2012), which makes it more likely to provide cloud-free images than other satellites in tropical regions. For the tropical mangroves, they are frequently covered by clouds (Wang et al., 2018a).

However, the Sentinel-2 data have one limitation—the radiometric

saturation effect—in evaluating mature and dense mangroves that usually have high biomass. This issue is a common drawback of multispectral imagery due to its limited penetration capability in forests. This problem also appears in this study, as shown in Fig. 6, where the biomasses greater than 250 Mg ha⁻¹ are underestimated. Future studies could use TanDEM-X as complementary data for mangrove forests with high AGB, as TanDEM-X can capture vertical information with an accuracy of 2 m (Sadeghi et al., 2018).

5.4. Field sample reduction

The limited number of ground samples available for model calibration and validation is a general problem in the development of a model for predicting biomass or other biophysical attributes of forests (Korhonen et al., 2017). For mangrove biomass estimation, most studies employed only 20–50 field sampling plots to calibrate the models and extrapolate them to the entire study area. Table 10 presents the numbers of field plots, mangrove areas, and remote sensing data reported by 11 selected studies that focused on mangrove biomass estimation. When biomass estimates are carried out at regional or larger scales, the number of field plots should increase to account for potential variations in various mangrove associations, as described in Asian et al. (2016) and Pham and Brabyn (2017).

Using the proposed G~ LiDAR~S2 model, approximately 39% of the field plot sampling work could be saved according to the comparison with the conventional G~S2 model in this work (Table 9 and Fig. 8). To collect the 39 (101·62 = 39) ground samples, a survey team of 3–4 people requires at least 4 day. While in 4 workdays, the UAV-LiDAR system (Velodyne VLP-16 Puck mounted on DJI M600 UAV) used in this study could fly 16–24 missions, namely, covering 640–960 ha when the same flight parameters employed in this study are used, and this UAV-LiDAR system might ideally generate 64,000–96,000 10 × 10 m LiDAR plots. The effectiveness of LiDAR and digital stereo imagery samplings in reducing field plots was qualitatively but not quantitatively described by previous studies (Korhonen et al., 2017; Puliti et al., 2018; Wulder et al., 2012). This paper is the first study that attempts to calculate the effectiveness of UAV-LiDAR as a linear bridge in reducing ground sampling work. However, caution must be taken when applying the findings to mangroves in other countries of the world.

Table 10

Summary of studies using field plots and remotely sensed data for mangrove biomass estimates.

References	Number of field plots	Mangrove area (ha)	Location	Auxiliary data
This study	97	2623	Hainan, China	UAV-LiDAR, Sentinel-2
Simard et al. (2006)	25	144,447	Florida, US	ALS, SRTM
Simard et al. (2008)	16	29,042	CGSM, Colombia	ICESat-GLAS, SRTM
Chadwick (2011)	38	230	Florida, US	ALS
Jachowski et al. (2013)	45	151	Ranong, Thailand	GeoEye-1, ASTER GDEM
Wicaksono et al. (2016)	40	446	Karimunjawa, Indonesia	ALOS AVNIR-2
Asian et al. (2016)	246 ^a	18,6292	Papua, Indonesia	SRTM
Castillo et al. (2017)	51	1216	Palawan, Philippines	Sentinel-1/2
Pham and Brabyn (2017)	140	~72,000	Cangio, Vietnam	SPOT-4/5
Pereira et al. (2018)	34	9000 ^b	Rio de Janeiro, Brazil	ALS
Pham et al. (2018)	25	< 2000	Hai Phong, Vietnam	ALOS-2 PALSAR-2, Sentinel-2
Fatoyinbo et al. (2018)	24	~7035	Zambezi Delta, Mozambique	ALS

^a Located in 41 transect plots of 0.5 ha each.^b The specific mangrove area was not reported.

5.5. UAV-LiDAR sampling intensity

Because the UAV-LiDAR collects only a small coverage of point clouds in one flight, the amount of required data, namely, the sampling intensity, not only determines the flight times of the UAV but also affects the AGB estimation accuracy. The decrease in the prediction accuracy in this study with the decrease in the UAV-LiDAR sampling intensity was expected because of the reduction in the LiDAR sample size used to fit the UAVLiDAR~S2 model (Fig. 9). Based on a comprehensive consideration of computation time and AGB retrieval accuracy, a 20% sampling intensity of the original LiDAR plots, namely, 2926 LiDAR plots, is also acceptable. The original LiDAR plots in this study covered approximately 146 ha of mangroves accounting for approximately 5.6% of the total mangrove area. Therefore, 20% of the original LiDAR samples accounted for only 1.12% of the total mangrove area. This result implies that for the entire mangrove area on northeast Hainan Island, we may need to collect representative and typical mangrove LiDAR point clouds over only approximately 1% of the area for mangrove AGB estimation.

Wulder et al. (2012) presented a selection of common LiDAR transect-based survey options, which are also suitable for UAV-LiDAR sample survey designs. The five common LiDAR sample survey designs are random lines, systematic lines, probability proportional to length of lines, stratified by panel with random lines, and stratified by land cover with random lines (Wulder et al., 2012). The fifth design may be the optimal choice for mangrove biomass assessment because it uses land cover to guide the transect layout to maximize the capture of forest attributes of interest (Wulder et al., 2012). However, this design needs to be modified to “stratified by mangrove species and height with random lines”. Meanwhile, the random lines should cover at least 1% of the mangroves.

5.6. The possibility of scale extrapolation

From the local scale to the regional scale, the accuracy of the G~LiDAR~S2 model is always better than that of the traditional G~S2 model, and the estimated accuracy increased (Fig. 6 and Table 7), which indicates that the point-line-polygon G~LiDAR~S2 model is suitable for large-scale mangrove AGB estimation. In the future, we will expand the model to the entire Hainan Island and probably to other mangrove provinces in China. At present, most of the studies that retrieved mangrove biomass cover small extents (Table 10). Large-scale mangrove biomass estimations are mainly based on a combination of SRTM and ICESAT-GLAS or ALS data, and these studies first uses ICESAT-GLAS or ALS data to calibrate SRTM data and produces a mangrove height map. Then, allometric equations are applied to the height map to calculate biomass (Fatoyinbo and Simard, 2013; Simard et al., 2008, 2006). The allometric equation that links mangrove height

to estimated biomass is derived from field plot measurements. Compared with this method, the proposed G~LiDAR~S2 model is simple and might produce higher prediction accuracy. Because linear bridges are employed, such as UAV-LiDAR, the vertical structure information of mangroves could be captured more accurately, even for the attributes of individual trees (Yin and Wang, 2019).

This study may pave the way for large-scale mangrove AGB estimation, especially in developing countries, where > 90% of the world's mangroves are distributed. With further decline in the cost of LiDAR sensors and the simplification of UAV operation, more developing countries could afford and employ UAV-LiDAR systems. For example, the UAV-LiDAR equipment used in this study cost only \$50,000. In the future, if the crowdsourced approach for field sampling and UAV-LiDAR acquisitions is used (Levin et al., 2017) or a remote UAV-LiDAR network is constructed, a global mangrove biomass map with high accuracy at 10 m spatial resolution is likely to be generated.

6. Conclusion

The main merit of this study is the first estimation of AGB in the mangrove forests on northeast Hainan Island in China using a newly developed upscaling method (G~LiDAR~S2) from field plots, UAV-LiDAR strip data and Sentinel-2 imagery based on a point-line-polygon framework. During this process, the partial-coverage UAV-LiDAR transects acted as a linear bridge to connect the field plots and the wall-to-wall Sentinel-2 data.

To examine the effectiveness of the upscaling method, this paper first tested the corresponding G~LiDAR~S2 model at a local scale (the QPR) and then extended it to the entire northeast Hainan Island, namely at the regional scale. The results indicated that the proposed G~LiDAR~S2 method ($R^2 = 0.62$ and RMSE = 50.36 Mg ha⁻¹) was superior to the traditional approach (named the G~S2 model), which directly linked field plots to Sentinel-2 data ($R^2 = 0.52$ and RMSE = 56.63 Mg ha⁻¹). The results also demonstrated that the proposed G~LiDAR~S2 model (UAV-LiDAR as the linear bridge) can significantly reduce field sampling work by approximately 39% in the study area. The results also revealed that the accuracy that was produced when only 20% of the UAV linear bridges were used was not significantly different from the accuracy that was produced when all UAV linear bridges were used. Overall, the proposed method produced a more accurate large-scale mangrove AGB estimation with reduced field plot measurements.

The results of this study indicated that northeast Hainan Island has a total mangrove AGB of 312,806.29 Mg with a mean AGB of 119.26 Mg ha⁻¹, which is higher than the mangrove AGB in other areas in China but lower than the global average value of mangrove AGB (184.8 Mg ha⁻¹).

The derived mangrove AGB map can serve as a baseline for future

mangrove studies, including those on biomass changes and mangrove responses to global warming and sea level rise in this region.

Acknowledgements

This study is supported by the National Key Research & Development (R&D) Plan of China (NO. 2017YFB0503600) and the National Science Foundation of China (NO. 41361090). We are very grateful to Dr. Baode Jiang from China University of Geosciences (Wuhan) and Feng Wan engineer for assisting in the acquisition of UAV-LiDAR data in field. The graduate student Xing Yang and undergraduate students Ling Tang and Zunqian Zhong from Hainan Normal University participated in the field survey.

References

- Asian, A., Rahman, A.F., Warren, M.W., Robeson, S.M., 2016. Mapping spatial distribution and biomass of coastal wetland vegetation in Indonesian Papua by combining active and passive remotely sensed data. *Remote Sens. Environ.* 183, 65–81.
- Blackburn, G.A., 1998. Spectral indices for estimating photosynthetic pigment concentrations: a test using senescent tree leaves. *Int. J. Remote Sens.* 19, 657–675.
- Bouvier, M., Durrieu, S., Fournier, R.A., Renaud, J.-P., 2015. Generalizing predictive models of forest inventory attributes using an area-based approach with airborne LiDAR data. *Remote Sens. Environ.* 156, 322–334.
- Breiman, L., 2001. Random forests. *Mach. Learn.* 45, 5–32.
- Castillo, J.A.A., Apan, A.A., Maraseni, T.N., Salmo, S.G., 2017. Estimation and mapping of above-ground biomass of mangrove forests and their replacement land uses in the Philippines using Sentinel imagery. *ISPRS J. Photogramm. Remote Sens.* 134, 70–85.
- Chadwick, J., 2011. Integrated LiDAR and IKONOS multispectral imagery for mapping mangrove distribution and physical properties. *Int. J. Remote Sens.* 32, 6765–6781.
- Chen, L., Wang, W., Zhang, Y., Lin, G., 2009. Recent progresses in mangrove conservation, restoration and research in China. *J. Plant Ecol.* 2, 45–54.
- Chowdhury, M.Q., Deb, J.C., Sonet, S.S., 2013. Timber species grouping in Bangladesh: linking wood properties. *Wood Sci. Technol.* 47, 797–813.
- Clough, B.F., Scott, K., 1989. Allometric relationships for estimating above-ground biomass in six mangrove species. *Forest Ecol. Manag.* 27, 117–127.
- Dash, J., Curran, P.J., 2004. The MERIS terrestrial chlorophyll index. *Int. J. Remote Sens.* 25, 5403–5413.
- Daughtry, C., Walthall, C., Kim, M., De Colstoun, E.B., McMurtrey III, J., 2000. Estimating corn leaf chlorophyll concentration from leaf and canopy reflectance. *Remote Sens. Environ.* 74, 229–239.
- Dong, W., Lan, J., Liang, S., Yao, W., Zhan, Z., 2017. Selection of LiDAR geometric features with adaptive neighborhood size for urban land cover classification. *Int. J. Appl. Earth Obs. Geoinf.* 60, 99–110.
- Drusch, M., Bello, U.D., Carlier, S., Colin, O., Fernandez, V., Gascon, F., Hoersch, B., Isola, C., Laberinti, P., Martimort, P., 2012. Sentinel-2: ESA's optical high-resolution mission for GMES operational services. *Remote Sens. Environ.* 120, 25–36.
- Duke, N.C., Meynecke, J.O., Dittmann, S., Ellison, A.M., Anger, K., Berger, U., Cannicci, S., Diele, K., Ewel, K.C., Field, C.D., 2007. A world without mangroves? *Science* 317, 41.
- Fan, K.-C., 2008. Population structure, allometry and above-ground biomass of Avicennia marina forest at the Chishui River Estuary, Tainan County, Taiwan. *J. For. Res.* 30, 1–15.
- Fatoyinbo, T., Feliciano, E.A., Lagomasino, D., Lee, S.K., Trettin, C., 2018. Estimating mangrove aboveground biomass from airborne LiDAR data: a case study from the Zambezi River delta. *Environ. Res. Lett.* 13, 12.
- Fatoyinbo, T.E., Simard, M., 2013. Height and biomass of mangroves in Africa from ICESat/GLAS and SRTM. *Int. J. Remote Sens.* 34, 668–681.
- Fernandez-Manso, A., Fernandez-Manso, O., Quintano, C., 2016. SENTINEL-2A red-edge spectral indices suitability for discriminating burn severity. *Int. J. Appl. Earth Obs. Geoinf.* 50, 170–175.
- Frampton, W.J., Dash, J., Watmough, G., Milton, E.J., 2013. Evaluating the capabilities of Sentinel-2 for quantitative estimation of biophysical variables in vegetation. *ISPRS J. Photogramm. Remote Sens.* 82, 83–92.
- Fromard, F., Puig, H., Mougin, E., Marty, G., Betoulle, J., Cadamuro, L., 1998. Structure, above-ground biomass and dynamics of mangrove ecosystems: new data from French Guiana. *Oecologia* 115, 39–53.
- Ghosh, S.M., Behera, M.D., 2018. Aboveground biomass estimation using multi-sensor data synergy and machine learning algorithms in a dense tropical forest. *Appl. Geogr.* 96, 29–40.
- Giri, C., Ochieng, E., Tieszen, L.L., Zhu, Z., Singh, A., Loveland, T., Masek, J., Duke, N., 2011. Status and distribution of mangrove forests of the world using earth observation satellite data. *Global Ecol. Biogeogr.* 20, 154–159.
- Gitelson, A.A., Gritz, Y., Merzlyak, M.N., 2003. Relationships between leaf chlorophyll content and spectral reflectance and algorithms for non-destructive chlorophyll assessment in higher plant leaves. *J. Plant Physiol.* 160, 271–282.
- Gregorutti, B., Michel, B., Saint-Pierre, P., 2017. Correlation and variable importance in random forests. *Stat. Comput.* 27, 659–678.
- Guo, Q., Su, Y., Hu, T., Zhao, X., Wu, F., Li, Y., Liu, J., Chen, L., Xu, G., Lin, G., Zheng, Y., Lin, Y., Mi, X., Fei, L., Wang, X., 2017. An integrated UAV-borne lidar system for 3D habitat mapping in three forest ecosystems across China. *Int. J. Remote Sens.* 38, 2954–2972.
- Hickey, S.M., Callow, N.J., Phinn, S., Lovelock, C.E., Duarte, C.M., 2018. Spatial complexities in aboveground carbon stocks of a semi-arid mangrove community: a remote sensing height-biomass-carbon approach. *Estuar. Coast. Shelf Sci.* 200, 194–201.
- Horler, D., DOCKRAY, M., Barber, J., 1983. The red edge of plant leaf reflectance. *Int. J. Remote Sens.* 4, 273–288.
- Hossain, M., Siddique, M.R.H., Saha, S., Abdullah, S.M.R., 2015. Allometric models for biomass, nutrients and carbon stock in Excoecaria agallocha of the Sundarbans, Bangladesh. *Wetl. Ecol. Manag.* 23, 765–774.
- Huang, H., Liu, C., Wang, X., Zhou, X., Gong, P., 2019. Integration of multi-resource remotely sensed data and allometric models for forest aboveground biomass estimation in China. *Remote Sens. Environ.* 221, 225–234.
- Huete, A., Didan, K., Miura, T., Rodriguez, E.P., Gao, X., Ferreira, L.G., 2002. Overview of the radiometric and biophysical performance of the MODIS vegetation indices. *Remote Sens. Environ.* 83, 195–213.
- Hutchison, J., Manica, A., Swetnam, R., Balmford, A., Spalding, M., 2014. Predicting global patterns in mangrove forest biomass. *Conserv. Lett.* 7, 233–240.
- Jachowski, N.R.A., Quak, M.S.Y., Friess, D.A., Duangnamon, D., Webb, E.L., Ziegler, A.D., 2013. Mangrove biomass estimation in Southwest Thailand using machine learning. *Appl. Geogr.* 45, 311–321.
- Ji, L., Zhang, L., Wylie, B., 2009. Analysis of dynamic thresholds for the normalized difference water index. *Photogramm. Eng. Remote Sens.* 75, 1307–1317.
- Jiang, L., Yang, D., Mei, L., Yang, X., 2018. Remote sensing estimation of carbon storage of mangrove communities in Shenzhen City. *Soc. Wetl. Sci. Bull.* 16, 618–625.
- Kamal, M., Phinn, S., Johansen, K., 2015. Object-based approach for multi-scale mangrove composition mapping using multi-resolution image datasets. *Remote Sens.* 7, 4753–4783.
- Komiyama, A., Poungparn, S., Kato, S., 2005. Common allometric equations for estimating the tree weight of mangroves. *J. Trop. Ecol.* 21, 471–477.
- Korhonen, L., Hadi, Packalen, P., Rautiainen, M., 2017. Comparison of Sentinel-2 and Landsat 8 in the estimation of boreal forest canopy cover and leaf area index. *Remote Sens. Environ.* 195, 259–274.
- Kuenzer, C., Bluemel, A., Gebhardt, S., Tuan Vo, Q., Dech, S., 2011. Remote sensing of mangrove ecosystems: a review. *Remote Sens. (Basel)* 3, 878–928.
- Kusmana, C., Hidayat, T., Tiryan, T., Rusdiana, O., Istomo, 2018. Allometric models for above- and below-ground biomass of Sonneratia spp. *Glob. Ecol. Conserv.* 15, e00417.
- Levin, N., Lechner, A.M., Brown, G., 2017. An evaluation of crowdsourced information for assessing the visitation and perceived importance of protected areas. *Appl. Geogr.* 79, 115–126.
- Liao, B., Zhang, Q., 2014. Area, distribution and species composition of mangroves in China. *Wetl. Sci.* 12, 435–440.
- Liu, J., Skidmore, A.K., Jones, S., Wang, T.J., Heurich, M., Zhu, X., Shi, Y.F., 2018a. Large off-nadir scan angle of airborne LiDAR can severely affect the estimates of forest structure metrics. *ISPRS J. Photogramm. Remote Sens.* 136, 13–25.
- Liu, K., Shen, X., Cao, L., Wang, G., Cao, F., 2018b. Estimating forest structural attributes using UAV-LiDAR data in Ginkgo plantations. *ISPRS J. Photogramm. Remote Sens.* 146, 465–482.
- Ma, Q., Su, Y., Guo, Q., 2017. Comparison of canopy cover estimations from airborne LiDAR, aerial imagery, and satellite imagery. *IEEE J. Sel. Top. Appl. Earth Obs. Remote Sens.* 10, 4225–4236.
- Matasci, G., Hermosilla, T., Wulder, M.A., White, J.C., Coops, N.C., Hobart, G.W., Zald, H.S.J., 2018. Large-area mapping of Canadian boreal forest cover, height, biomass and other structural attributes using Landsat composites and lidar plots. *Remote Sens. Environ.* 209, 90–106.
- Mura, M., Bottalico, F., Giannetti, F., Bertani, R., Giannini, R., Mancini, M., Orlandini, S., Travagliani, D., Chirici, G., 2018. Exploiting the capabilities of the Sentinel-2 multi spectral instrument for predicting growing stock volume in forest ecosystems. *Int. J. Appl. Earth Obs. Geoinf.* 66, 126–134.
- Mutanga, O., Skidmore, A.K., 2004. Narrow band vegetation indices overcome the saturation problem in biomass estimation. *Int. J. Remote Sens.* 25, 3999–4014.
- Nelson, R., Margolis, H., Montesano, P., Sun, G., Cook, B., Corp, L., Andersen, H.-E., Pellatt, F.P., Fickel, T., Kauffman, J., 2017. Lidar-based estimates of aboveground biomass in the continental US and Mexico using ground, airborne, and satellite observations. *Remote Sens. Environ.* 188, 127–140.
- Ong, J.E., Gong, W.K., Wong, C.H., 2004. Allometry and partitioning of the mangrove, Rhizophora apiculata. *Forest Ecol. Manag.* 188, 395–408.
- Owers, C.J., Rogers, K., Woodroffe, C.D., 2018. Terrestrial laser scanning to quantify above-ground biomass of structurally complex coastal wetland vegetation. *Estuar. Coast. Shelf Sci.* 204, 164–176.
- Pereira, F.R.D.S., Kampel, M., Soares, M.L.G., Estrada, G.C.D., Bentz, C., Vincent, G., 2018. Reducing uncertainty in mapping of mangrove aboveground biomass using airborne discrete return Lidar data. *Remote Sens.* 10, 637.
- Pham, L.T.H., Brabyn, L., 2017. Monitoring mangrove biomass change in Vietnam using SPOT images and an object-based approach combined with machine learning algorithms. *ISPRS J. Photogramm. Remote Sens.* 128, 86–97.
- Pham, T.D., Yoshino, K., Le, N.N., Bui, D.T., 2018. Estimating aboveground biomass of a mangrove plantation on the Northern coast of Vietnam using machine learning techniques with an integration of ALOS-2 PALSAR-2 and Sentinel-2A data. *Int. J. Remote Sens.* 1–28.
- Polewski, P., Yao, W., Cao, L., Gao, S., 2019. Marker-free coregistration of UAV and backpack LiDAR point clouds in forested areas. *ISPRS J. Photogramm. Remote Sens.* 147, 307–318.
- Puliti, S., Ene, L.T., Gobakken, T., Næsset, E., 2017. Use of partial-coverage UAV data in sampling for large scale forest inventories. *Remote Sens. Environ.* 194, 115–126.
- Puliti, S., Saarela, S., Gobakken, T., Stahl, G., Næsset, E., 2018. Combining UAV and

- Sentinel-2 auxiliary data for forest growing stock volume estimation through hierarchical model-based inference. *Remote Sens. Environ.* 204, 485–497.
- Sadeghi, Y., St-Onge, B., Leblon, B., Prieur, J.F., Simard, M., 2018. Mapping boreal forest biomass from a SRTM and TanDEM-X based on canopy height model and Landsat spectral indices. *Int. J. Appl. Earth Obs. Geoinf.* 68, 202–213.
- Saenger, P., Snedaker, S.C., 1993. Pantropical trends in mangrove above-ground biomass and annual litterfall. *Oecologia* 96, 293–299.
- Shao, Z., Fu, H., Li, D., Altan, O., Cheng, T., 2019. Remote sensing monitoring of multi-scale watersheds impermeability for urban hydrological evaluation. *Remote Sens. Environ.* 232 111338.
- Shao, Z.F., Zhang, L.J., Wang, L., 2017. Stacked sparse autoencoder modeling using the synergy of airborne LiDAR and satellite optical and SAR data to map forest above-ground biomass. *IEEE J. Sel. Top. Appl. Earth Obs. Remote Sens.* 10, 5569–5582.
- Shi, Y., Wang, T., Skidmore, A.K., Heurich, M., 2018. Important LiDAR metrics for discriminating forest tree species in Central Europe. *ISPRS J. Photogramm. Remote Sens.* 137, 163–174.
- Shoko, C., Mutanga, O., 2017. Examining the strength of the newly-launched Sentinel 2 MSI sensor in detecting and discriminating subtle differences between C3 and C4 grass species. *ISPRS J. Photogramm. Remote Sens.* 129, 32–40.
- Simard, M., Rivera-Monroy, V.H., Mancera-Pineda, J.E., Castañeda-Moya, E., Twilley, R.R., 2008. A systematic method for 3D mapping of mangrove forests based on Shuttle Radar Topography Mission elevation data, ICEsat/GLAS waveforms and field data: application to Ciéaga Grande de Santa Marta, Colombia. *Remote Sens. Environ.* 112, 2131–2144.
- Simard, M., Zhang, K., Rivera-Monroy, V.H., Ross, M.S., Ruiz, P.L., Castañeda-Moya, E., Twilley, R.R., Rodriguez, E., 2006. Mapping height and biomass of mangrove forests in Everglades National Park with SRTM elevation data. *Photogramm. Eng. Remote Sci.* 72, 299–311.
- Su, Y., Guo, Q., Xue, B., Hu, T., Alvarez, O., Tao, S., Fang, J., 2016. Spatial distribution of forest aboveground biomass in China: estimation through combination of spaceborne lidar, optical imagery, and forest inventory data. *Remote Sens. Environ.* 173, 187–199.
- Tam, N.F.Y., Wong, Y.S., Lan, C.Y., Chen, G.Z., 1995. Community structure and standing crop biomass of a mangrove forest in Futian Nature Reserve, Shenzhen, China. *Hydrobiologia* 295, 193–201.
- Valderrama-Landeros, L., Flores-de-Santiago, F., Kovacs, J.M., Flores-Verdugo, F., 2018. An assessment of commonly employed satellite-based remote sensors for mapping mangrove species in Mexico using an NDVI-based classification scheme. *Environ. Monit. Assess.* 190, 13.
- Wang, D., Wan, B., Qiu, P., Su, Y., Guo, Q., Wang, R., Sun, F., Wu, X., 2018a. Evaluating the performance of Sentinel-2, landsat 8 and Pléiades-1 in mapping mangrove extent and species. *Remote Sens.* 10, 1468.
- Wang, L., Jia, M., Yin, D., Tian, J., 2019. A review of remote sensing for mangrove forests: 1956–2018. *Remote Sens. Environ.* 231 111223.
- Wang, M., Cao, W.Z., Guan, Q.S., Wu, G.J., Wang, F.F., 2018b. Assessing changes of mangrove forest in a coastal region of southeast China using multi-temporal satellite images. *Estuar. Coast. Shelf Sci.* 207, 283–292.
- Wen, Y., 1999. Biomass and productivity of five mangrove communities in Yingluo Bay of Guangxi. *Guangxi Sci.* 63–68.
- Wicaksono, P., Danoedoro, P., Hartono, Nehren, U., 2016. Mangrove biomass carbon stock mapping of the Karimunjawa Islands using multispectral remote sensing. *Int. J. Remote Sens.* 37, 26–52.
- Wulder, M.A., White, J.C., Nelson, R.F., Næsset, E., Ørka, H.O., Coops, N.C., Hilker, T., Bater, C.W., Gobakken, T., 2012. Lidar sampling for large-area forest characterization: a review. *Remote Sens. Environ.* 121, 196–209.
- Yan, W.Y., Shaker, A., 2018. Airborne LiDAR intensity banding: cause and solution. *ISPRS J. Photogramm. Remote Sens.* 142, 301–310.
- Yin, D., Wang, L., 2019. Individual mangrove tree measurement using UAV-based LiDAR data: possibilities and challenges. *Remote Sens. Environ.* 223, 34–49.
- Zhao, X., Guo, Q., Su, Y., Xue, B., 2016. Improved progressive TIN densification filtering algorithm for airborne LiDAR data in forested areas. *ISPRS J. Photogramm. Remote Sens.* 117, 79–91.
- Zhu, Y., Liu, K., Liu, L., Myint, S., Wang, S., Liu, H., He, Z., 2017. Exploring the potential of WorldView-2 red-edge band-based vegetation indices for estimation of mangrove leaf area index with machine learning algorithms. *Remote Sens.* 9, 1060.
- Zhu, Y., Liu, K., Liu, L., Wang, S., Liu, H., 2015. Retrieval of mangrove aboveground biomass at the individual species level with WorldView-2 images. *Remote Sens.* 7, 12192–12214.